On the biophysics and kinetics of toehold-mediated DNA strand displacement *Supplementary Information*

Niranjan Srinivas,[*,†] Thomas E. Ouldridge,[*,‡] Petr Šulc,[‡] Joseph M. Schaeffer,[†] Bernard Yurke,[¶] Ard A. Louis,[‡] Jonathan P. K. Doye[§] and Erik Winfree[†]

[*]Both these authors contributed equally to this work.
Email: niranjan@caltech.edu, t.ouldridge1@physics.ox.ac.uk
[†]California Institute of Technology, 1200 E California Blvd., Pasadena, CA - 91125
[‡]Rudolph Peierls Centre for Theoretical Physics, 1 Keble Road, Oxford, UK, OX1 3NP
[¶] Boise State University, 1910 University Dr., Boise, ID - 83725
[§]Physical and Theoretical Chemistry Laboratory, South Parks Road, Oxford, UK, OX1 3QZ

S1 Introduction

The phenomenological model of Zhang and Winfree (1) directly treats reversible toehold exchange (Figure S1), which is a generalization of strand displacement. In the main text, we restricted their model to irreversible strand displacement without any fundamental changes.

S2 Intuitive Energy Landscape model

Zero toehold case. The IEL for the zero toehold case ($h = 0$) is illustrated in Figure S2. The main modification is the addition of a fraying step (state A to A′, at the cost of one base pair stack - $|\Delta G_{\rm bp}|$), which permits a collision leading to the formation of a base pair between the substrate-incumbent duplex and the invader. Such a collision essentially results in the displacement of one incumbent base by the invader (state B′). The remaining states are identical to the case with a toehold at least 1-base long, except that the branch migration domain is shorter by one base (length $b-1$ rather than b). Since the substrate-incumbent duplex needs to fray at either end to permit strand displacement from that end, the collision rate includes a multiplicative factor of $2\times e^{-|\Delta G_{\rm bp}|/RT}$, which accounts for the average fraction of duplexes frayed at either end. So, the complexes join at a rate $k_{\rm bi}\times u\times(2\times e^{-|\Delta G_{\rm bp}|/RT})$ rather than just $k_{\rm bi}\times u$, where u is the concentration.

We now approximate $k_{\rm eff}(0)$ in terms of $k_{\rm eff}(1)$, which will prove useful once we derive expressions for $k_{\rm eff}(h)$ for $h>0$. As we pointed out earlier, once the first base pair forms between the frayed substrate-incumbent duplex and the invader, the situation is identical to the $h=1$ case with the toehold just bound, except with a branch migration domain of length $b-1$ rather than b. Assuming b is long enough that $b-1\approx b$,

$$k_{\rm eff}(0)\approx(2\ e^{-|\Delta G_{\rm bp}|/RT})\ k_{\rm eff}(1)\quad . \tag{1}$$

Choosing $\mathbf{k_{uni}}$. We choose $k_{\rm uni}$ such that the rate of dissociation of the last base pair of the toehold is approximately equal to the rate of fraying of every other base pair. So, we set

$$k_{\rm uni}\ e^{-|\Delta G_{\rm bp}|/RT}\approx k_{\rm bi}\ e^{(-|\Delta G_{\rm bp}|+|\Delta G_{\rm assoc}|)/RT}\ u_0, \tag{2}$$

which yields

$$k_{\rm uni}\approx k_{\rm bi}\ e^{|\Delta G_{\rm assoc}|/RT}\ u_0 \tag{3}$$

where $u_0=1$ M is the reference concentration.

Modeling $\mathbf{k_{eff}}$. Conceptually, we may split the kinetics of strand displacement into two parts: the concentration-dependent, bimolecular part involving collision and formation of the first base pair of the toehold (state A to B) and the unimolecular part comprising the formation of the remaining base pairs of the toehold (states B to C) and branch migration (states C to F). The unimolecular part is modeled as a random walk on the free energy landscape starting at B, and ending either at A (no displacement) or at E (successful displacement). In the low-concentration regime, the unimolecular part finishes (one way or the other) much faster than the rate of collision; so, we model the effective rate constant of strand displacement, $k_{\rm eff}$, as

$$k_{\rm eff}=k_v\times p \tag{4}$$

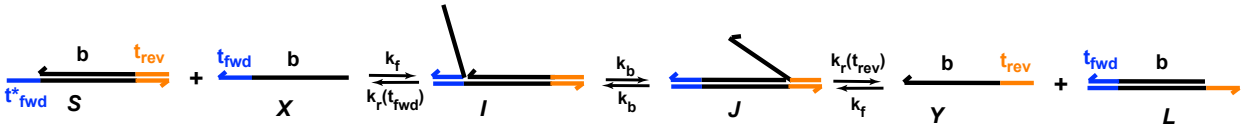

Figure S1: The phenomenological model of Zhang and Winfree (1) for reversible toehold exchange. For simplicity, they assume the hybridization rate constants for both toeholds to be the same (k_f). k_f and k_b are fitted to the data.

where k_v is the rate constant for the formation of the first toehold base pair and $p = \mathbb{P}$(reaching E before A starting at B) is the probability of successful displacement starting at B. Since the IEL assumes a collision rate of $k_{\text{bi}} \times u$, $k_v = k_{\text{bi}}$.

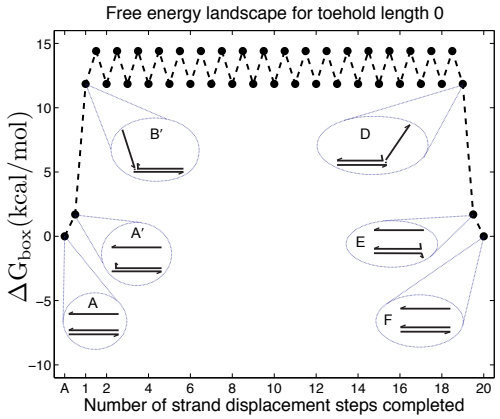

Figure S2: IEL free energy landscape at 25 °C for a 0-base toehold. First, the invader and the substrate-incumbent complex are unconstrained by each other (A). Then, the substrate-incumbent complex frays at one end (A′). This fraying step, at the cost of one base pair stack ($|\Delta G_{\text{bp}}|$), is necessary to enable a collision leading to a base pair, since no toehold is present. Once such a collision occurs, the first base of the incumbent has effectively been displaced by the invader (B′). The remaining states are identical to the positive toehold case.

Calculating p. First, given the rates of the individual transitions as specified in the kinetic model, the probabilities of transition from each state to its neighbors can be calculated. Let $p_{i,j}$ be the probability of going from state i to state j. Then, we choose

$$p_{i,i+1} = \frac{k_{i,i+1}}{k_{i,i+1} + k_{i,i-1}} \quad , \tag{5}$$

$$p_{i,i-1} = \frac{k_{i,i-1}}{k_{i,i+1} + k_{i,i-1}} \quad . \tag{6}$$

Since we are interested in the probability that the random walk finishes at one end rather than the other, we use absorbing boundaries:

$$p_{i,i} = 1 \text{ for } i = \text{A, E } (\text{A}' \text{ for 0 toehold}) \; . \tag{7}$$

Given these transition probabilities, p can be calculated analytically using the method of Rudolph (2) for calculating absorption probabilities for a 1-dimensional random walk with absorbing boundaries.

Alternate unimolecular rate model. We also considered the Kawasaki (3) method for assigning unimolecular transition rates in the IEL:

$$k_{ij} = k_{\text{uni}} \times \mathrm{e}^{-(\Delta G_{\text{box}}(j) - \Delta G_{\text{box}}(i))/2RT} \tag{8}$$

$$k_{ji} = k_{\text{uni}} \times \mathrm{e}^{-(\Delta G_{\text{box}}(i) - \Delta G_{\text{box}}(j))/2RT} \tag{9}$$

As with the Metropolis rate model, this choice guarantees detailed balance and thus that the system eventually converges to a Boltzmann distribution:

$$\text{Prob}(i) = \frac{1}{Q}\mathrm{e}^{-\frac{\Delta G_{\text{box}}(i)}{RT}} \quad \text{where} \quad Q = \sum_i \mathrm{e}^{-\frac{\Delta G_{\text{box}}(i)}{RT}} .$$

Once again, we choose k_{uni} such that the rate of dissociation of the last base pair of the toehold is approximately equal to the rate of fraying of every other base pair. For the Kawasaki method, we have

$$k_{\text{uni}}\; e^{-|\Delta G_{\text{bp}}|/2RT} \approx k_{\text{bi}}\; e^{(-|\Delta G_{\text{bp}}| + |\Delta G_{\text{assoc}}|)/RT}\; u_0, \tag{10}$$

which yields

$$k_{\text{uni}} \approx k_{\text{bi}} \times e^{(-|\Delta G_{\text{bp}}|/2\; +\; |\Delta G_{\text{assoc}}|)/RT}\; u_0 \; . \tag{11}$$

With $k_{\text{uni}} \approx 1.8 \times 10^7$ /s as calculated above, the Kawasaki method consistently predicts a slightly smaller acceleration in k_{eff} with toehold length than the Metropolis (4) method (see Figure S3); therefore our conclusions about constraints on IEL parameters that are necessary to match experimental data are robust to this choice. In the analysis below, the Metropolis method is assumed throughout.

Analytical approximations for $k_{\text{eff}}(h)$. The IEL is simple enough to yield itself to an approximate analysis that permits intuitive understanding of the model. For $h > 1$, we may approximate $k_{\text{eff}}(h)$ as:

$$k_{\text{eff}}(h) \approx k_{\text{bi}} \times p_{\text{zip}} \times p_{\text{bm|toe}}(h) \tag{12}$$

where p_{zip} is the probability that the full toehold "zips up" once the first base pair is formed, $k_{\text{bi}} \times p_{\text{zip}}$ is the bimolecular rate constant for all the base pairs in the toehold to form and $p_{\text{bm|toe}}(h)$ is the probability that, once the toehold has zipped up, the incumbent is displaced before the toehold dissociates.

For $h = 1$, there are no other bases in the toehold to zip up, so $k_{\text{eff}}(1)$ may simply be approximated as

$$k_{\text{eff}}(1) \approx k_{\text{bi}} \times p_{\text{bm|toe}}(1). \tag{13}$$

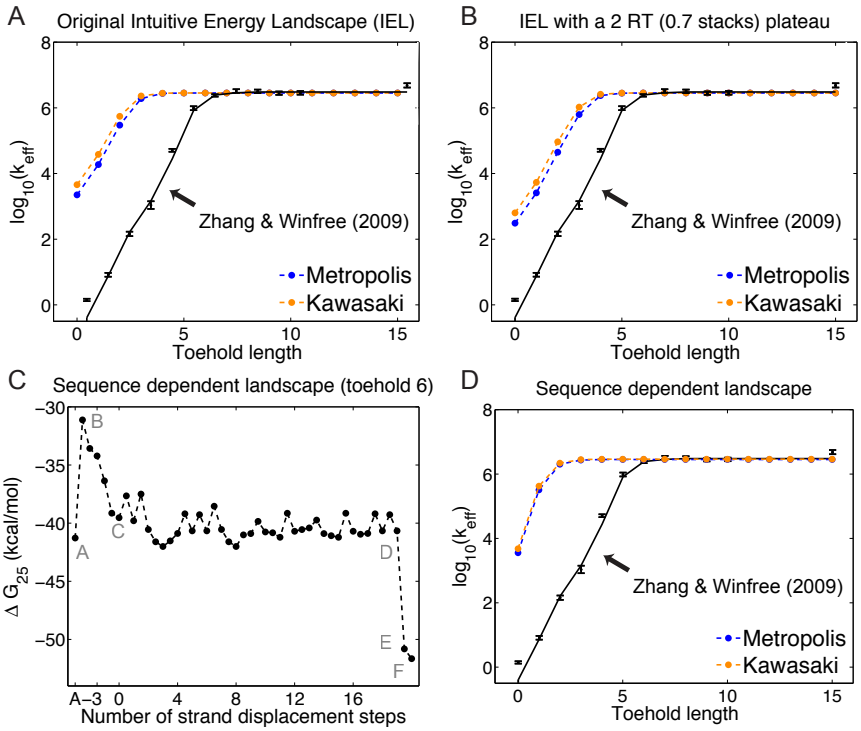

Figure S3: Strand displacement kinetics predicted by the IEL under varying conditions, for both Metropolis and Kawasaki unimolecular rate models. (A) IEL (2.6, 0) (B) IEL (2.6, 1.2) (D) for the sequence dependent free energy landscape predicted by the NUPACK energy model with Dangles = "Some" (shown in (C)). None of these variations is consistent with experimental data (1). (C) States A–F pertain to Figure 3 in the main text. The sequence dependent landscape is much "rougher" than the IEL, but this "roughness" goes no further in accounting for the data (D).

We shall now estimate $p_{\mathrm{bm|toe}}(h)$. Let k_{first} be the rate at which the first base of the incumbent is displaced by the invader, once the toehold is bound. Let $k_r(h)$ be the rate at which the toehold of length h dissociates from the state in which it is fully bound (i.e. state C of Figure 3 in the main text). We estimate k_{first} and $k_r(h)$ later. The probability of displacing the first base of the incumbent before the toehold dissociates is simply $k_{\mathrm{first}}/(k_{\mathrm{first}} + k_r(h))$.

For simplicity, we assume that once $(b-1)$ bases of the incumbent have been displaced, the last base always dissociates. This approximation allows us to think about branch migration as a flat random walk. Our approximation is reasonable because the probability that the invader dissociates without completing strand displacement after displacing $(b-1)$ bases of the incumbent can only be 0.5, in the worst case (for a 0-base toehold, with $k_{\mathrm{uni}} >> k_{\mathrm{bi}}$), and hence introduces negligible error on a logarithmic scale. Moreover, if branch migration is indeed significantly slow relative to fraying, we would expect that the last few bases of the incumbent would fray, leading to the dissociation of the incumbent even before branch migration completes. Once the first base of the incumbent has been displaced, the probability of displacing the remaining bases of the incumbent before going back to the toehold-only-bound state is $1/(b-1)$, according to the gambler's ruin analysis (see Section 14.2 of Feller (5)). With a probability of $(b-2)/(b-1)$, we return to the toehold bound state - from where, by definition, displacement succeeds with a probability of $p_{\mathrm{bm|toe}}(h)$.

Therefore, we have $p_{\mathrm{bm|toe}}(h) \approx$

$$\left(\frac{k_{\mathrm{first}}}{k_{\mathrm{first}} + k_r(h)}\right)\left[\frac{1}{b-1} + \frac{b-2}{b-1} \times p_{\mathrm{bm|toe}}(h)\right] \quad (14)$$

which yields

$$p_{\mathrm{bm|toe}}(h) \approx \frac{k_{\mathrm{first}}}{k_{\mathrm{first}} + (b-1)k_r(h)} \ . \quad (15)$$

Therefore, equation 12 yields

$$k_{\mathrm{eff}}(h) \approx k_{\mathrm{bi}} \times p_{\mathrm{zip}} \times \frac{k_{\mathrm{first}}}{k_{\mathrm{first}} + (b-1)k_r(h)} \ . \quad (16)$$

With some algebra, equation 16 yields

$$k_{\mathrm{eff}}(h) \approx \frac{k_{\mathrm{bi}} \times p_{\mathrm{zip}}}{1 + (b-1)\frac{k_r(h)}{k_{\mathrm{first}}}} \quad (17)$$

for $h > 1$.

Analyzing equation 17 provides intuition about the dependence of $k_{\text{eff}}(h)$ on h. For long toeholds, i.e. in the saturation limit, $(b-1)\ \frac{k_r(h)}{k_{\text{first}}} << 1$; this yields the saturation value

$$k_{\text{eff}}(\infty) \approx k_{\text{bi}} \times p_{\text{zip}}. \tag{18}$$

For short toeholds, i.e in the "sloping" part of the $k_{\text{eff}}(h)$ curve, $(b-1)\ \frac{k_r(h)}{k_{\text{first}}} >> 1$ and this yields

$$k_{\text{eff}}(h) \approx \frac{k_{\text{bi}}\ p_{\text{zip}}\ k_{\text{first}}}{(b-1)\ k_r(h)}. \tag{19}$$

We now estimate p_{zip}. For $h > 1$, we assume, for simplicity, that the formation of a second base pair of the toehold will guarantee zippering. Then, p_{zip} may be approximated as

$$p_{\text{zip}} \approx \frac{k_{\text{uni}}}{k_{\text{uni}} + k_r(1)}\ . \tag{20}$$

Note that $k_r(1)$ is just the rate for the simple bimolecular dissociation step, and so we have

$$k_r(1) \approx k_{\text{bi}}\ \lambda \tag{21}$$

where λ is defined as

$$\lambda = e^{-(|\Delta G_{\text{bp}}| - \Delta G_{\text{assoc}})/RT}\ u_0\ . \tag{22}$$

We now estimate $k_r(h)$ for $h > 1$. Once a toehold of length h is fully bound, $(h-1)$ uphill fraying steps and 1 dissociation step need to occur for the toehold to dissociate. Therefore,

$$k_r(h) \approx k_{\text{fray}}(h-1) \times (1 - p_{\text{zip}}) \tag{23}$$

where $k_{\text{fray}}(h-1)$ is the rate at which $(h-1)$ base pairs of the toehold fray, starting from the toehold fully bound state, to leave the invader bound by 1 base of the toehold (state C to B in Figure 3 in the main text).

Clearly,

$$k_{\text{fray}}(h-1) = k_{\text{uni}}\ e^{-(h-1)\ |\Delta G_{\text{bp}}|/RT}. \tag{24}$$

From equations 20, 23 and 24, we get

$$k_r(h) \approx e^{-(h-1)\ |\Delta G_{\text{bp}}|/RT} \times \frac{1}{1/k_{\text{uni}} + 1/k_r(1)}\ . \tag{25}$$

We also recall that in our particular parameterization we chose k_{uni} such that $k_r(1) \approx k_{\text{fray}}(1)$, although we do not use or need that condition in this analysis.

Lastly,

$$k_{\text{first}} = \frac{1}{2} \times k_{\text{uni}} \times e^{-\Delta G_{s+p}/RT} \tag{26}$$

where ΔG_{s+p} is defined as

$$\Delta G_{s+p} = \Delta G_s + \Delta G_p \tag{27}$$

and ΔG_s is the sawtooth amplitude and ΔG_p is the plateau height.

Substituting for $k_r(h)$ from equation 25, k_{first} from equation 26 and p_{zip} from equation 20 into equation 19, we may approximate $k_{\text{eff}}(h)$ for $h > 1$ in the pre-saturation regime. We also assume that b is long enough that $b - 1 \approx b$. With some algebra, we get

$$k_{\text{eff}}(h) \approx \frac{k_{\text{uni}}\ e^{-(\Delta G_{s+p} - h|\Delta G_{\text{bp}}|)/RT}\ \eta}{2\ b} \tag{28}$$

where η is defined as

$$\eta = \frac{1}{e^{\Delta G_{\text{assoc}}/RT}\ u_0}. \tag{29}$$

We now approximate $k_{\text{eff}}(1)$ using equation 13. Using equations 15, 21 and 26, we get

$$k_{\text{eff}}(1) \approx \frac{\rho\ k_{\text{bi}}}{\rho + 2\ b\ \lambda\ e^{\Delta G_{s+p}/RT}} \tag{30}$$

where ρ is defined as

$$\rho = k_{\text{uni}}/k_{\text{bi}}. \tag{31}$$

Having already assumed that $b-1 \approx b$, we may approximate $k_{\text{eff}}(0)$ in terms of $k_{\text{eff}}(1)$ using equation 1. Along with equation 30, this yields

$$k_{\text{eff}}(0) \approx \frac{2\ e^{-|\Delta G_{\text{bp}}|/RT}\ \rho\ k_{\text{bi}}}{\rho + 2\ b\ \lambda\ e^{\Delta G_{s+p}/RT}}\ . \tag{32}$$

Although equations 30 and 32 seem different in form from equation 28, that is only because equation 28 assumes the pre-saturation ("sloping") regime, whereas equations 30 and 32 are more general. For reasonable values of ρ and long enough b, such as the default IEL values ($\rho \approx 25, b = 20$), we may use the approximation

$$\rho + 2\ b\ \lambda\ e^{\Delta G_{s+p}/RT} \approx 2\ b\ \lambda\ e^{\Delta G_{s+p}/RT}. \tag{33}$$

This yields

$$k_{\text{eff}}(1) \approx \frac{k_{\text{uni}}\ e^{-(\Delta G_{s+p} - |\Delta G_{\text{bp}}|)/RT}\ \eta}{2\ b} \tag{34}$$

and

$$k_{\text{eff}}(0) \approx \frac{k_{\text{uni}}\ e^{-\Delta G_{s+p}/RT}\ \eta}{b} \tag{35}$$

which are consistent in form with equation 28, but for the factor of two for $h = 0$.

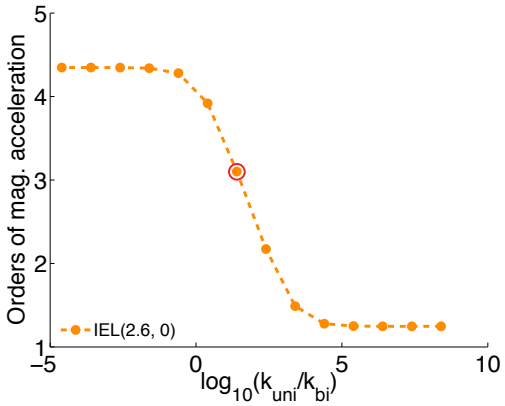

Figure S4: The influence of $k_{\text{uni}}/k_{\text{bi}}$ on the orders of magnitude acceleration in k_{eff} between toehold lengths 15 and 0 ($\mathcal{A}_{15,0}$) predicted by IEL(2.6, 0). The red circle indicates the default value of $k_{\text{uni}}/k_{\text{bi}}$. The IEL exhibits sigmoidal response to $\log_{10}(k_{\text{uni}}/k_{\text{bi}})$ and even implausibly low values of $k_{\text{uni}}/k_{\text{bi}}$ do not result in acceleration that matches the experimentally observed value of 6.5 orders of magnitude.

We define

$$\mathcal{A}_{h_2,h_1} = \log_{10}(k_{\text{eff}}(h_1)) - \log_{10}(k_{\text{eff}}(h_2)) \tag{36}$$

to be the orders of magnitude acceleration in k_{eff} as toehold length increases from h_1 to h_2. We now use equations 18 and 32 to study the dependence of $\mathcal{A}_{\infty,0}$ on ρ, ΔG_{s+p} and b. With some algebra, equations 18 and 32 yield

$$\mathcal{A}_{\infty,0} \approx \mu + \log_{10}\left(\frac{\rho + 2\ b\ \lambda\ e^{\Delta G_{s+p}/RT}}{\rho + \lambda}\right) \tag{37}$$

where μ is defined as

$$\mu = \log_{10}\left(e^{|\Delta G_{\text{bp}}|/RT}/2\right) \approx 0.9\ . \tag{38}$$

Dependence on $\rho = \mathbf{k_{uni}/k_{bi}}$. To analyze the effect of changing ρ on $\mathcal{A}_{\infty,0}$, let us choose a priori reasonable values for the other parameters: $b = 20$, $\Delta G_s = 1.5$ stacks (2.6 kcal/mol) and $\Delta G_p = 0$. Then, equation 37 becomes

$$\mathcal{A}_{\infty,0} \approx 0.9 + \log_{10}\left(\frac{\rho + 4000}{\rho + 1.4}\right) \tag{39}$$

whose behavior is qualitatively similar to the numerical curve plotted in Figure S4. Moreover, the difference between $\mathcal{A}_{\infty,0}$ at $\rho = \infty$ and $\rho = 0$ as predicted by equation 39 is approximately 3.5, which is consistent with the total variation in $\mathcal{A}_{15,0}$ as numerically plotted in Figure S4.

Dependence on $\mathbf{\Delta G_{s+p}}$. For the default k_{uni} and k_{bi} values used in the IEL, $\rho/(\rho + \lambda)$ may be neglected in equation 37 to yield

$$\mathcal{A}_{\infty,0} \approx \mu + \log_{10}\left(\frac{2\ b\ e^{\Delta G_{s+p}/RT}\ \lambda}{\rho + \lambda}\right)\ . \tag{40}$$

This yields an approximately linear dependence on ΔG_{s+p}:

$$\mathcal{A}_{\infty,0} \approx c_1 + c_2\ \Delta G_{s+p} \tag{41}$$

where

$$c_1 = \mu + \log_{10}\left(\frac{2\ b\ \lambda}{\rho + \lambda}\right) \tag{42}$$

and

$$c_2 = \frac{1}{RT\log_e(10)}. \tag{43}$$

Dependence on b. From equation 40, we have

$$\mathcal{A}_{\infty,0} \approx \log_{10}(b) + c_3 \tag{44}$$

where

$$c_3 = \mu + \log_{10}\left(\frac{2\ e^{\Delta G_{s+p}/RT}\ \lambda}{\rho + \lambda}\right)\ . \tag{45}$$

The logarithmic dependence of $\mathcal{A}_{\infty,0}$ on b is qualitatively similar to the numerical curve of $\mathcal{A}_{15,0}$ plotted in Figure S5.

Estimating branch migration step times. In order to compare with experimentally inferred values (6, 7), we define average branch migration step time (t_{bm}) as the average time taken for a single step of branch migration in either direction. For the IEL and AEL, t_{bm} is calculated as

$$t_{\text{bm}} = \frac{1}{k_{\text{bm}}} \tag{46}$$

where

$$k_{\text{bm}} = k_{\text{uni}} \times e^{-\Delta G_s/RT}. \tag{47}$$

S3 Augmented Energy Landscape model

The IEL assumes the initial attachment of all toeholds occurs at the same rate. It is possible to consider alternatives, such as an attachment rate that is

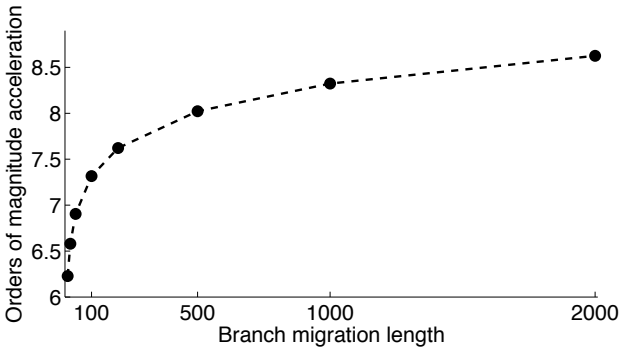

Figure S5: Orders of magnitude acceleration in k_{eff} between toehold lengths 15 and 0 ($\mathcal{A}_{15,0}$), as a function of the length of the branch migration domain, as predicted by IEL(5.3, 2.0).

linear in toehold length. At the cost of some of its intuitive simplicity, the IEL can be augmented to include such a linear dependence of the binding rate on toehold length. We outline the Augmented Energy Landscape model (AEL) below. The state space of the model is identical to the IEL, although we now include a multiplicity factor in the free energy of states with a partially formed toehold. This accounts for the fact that there are several ways in which to form an incomplete toehold. Note that the AEL represents the 0-base toehold system in an identical fashion to the IEL.

Free-energy model. The AEL free-energy model is identical to that of the IEL except for states in which the toehold is partially formed. We adjust the free energy of these states by a factor

$$\Delta G_{\text{mult}}(n) = -RT \ln(h - n + 1), \tag{48}$$

where n is the number of base pairs present and h is the total toehold length. This factor accounts for the multiplicity of states with n base pairs (assuming the toehold base pairs form a continuous helix).

Rate model. The AEL has an identical rate model to the IEL, except for transitions involving states in which the toehold is partially formed. The transition from n to $n-1$ base pairs with the toehold could occur by fraying a base pair at either end of the partially formed duplex. We therefore assign these processes a rate

$$k_{n,n-1} = 2k_{\text{uni}}\ \mathrm{e}^{-|\Delta G_{\text{bp}}|/RT}\quad . \tag{49}$$

The requirement of detailed balance fixes the rates in the opposite direction:

$$k_{n-1,n} = 2k_{\text{uni}}\frac{h+1-n}{h+2-n}. \tag{50}$$

Attachment to the toehold is assumed to occur in h equally likely ways: the rate of attachment is then

$$k_{0,1} = h\, k_{\text{bi}}\, u_0\ \mathrm{e}^{-\Delta G_{\text{volume}}/RT}, \tag{51}$$

where $u_0 = 1$ M is the reference concentration. Once again, detailed balance fixes the reverse rate.

$$k_{1,0} = k_{\text{bi}}\, u_0\ \mathrm{e}^{(-|\Delta G_{\text{bp}}|+\Delta G_{\text{assoc}})/RT}\quad . \tag{52}$$

The remaining consideration is the relation between k_{uni} and k_{bi}. Once again, we assume that breaking of the final base pair in the toehold occurs at the same rate as other base pairs are disrupted, giving

$$k_{\text{uni}} = k_{\text{bi}} u_0\ \mathrm{e}^{\Delta G_{\text{assoc}}/RT}\quad . \tag{53}$$

The AEL is simulated in a manner exactly analogous to Multistrand (see Supplementary Section S4), using a Gillespie algorithm (8) and utilizing "first step" mode in which the strands are initialized in the state with 1 base pair, and the system is evolved to see if displacement is successful. The success probability is then multiplied by the initial binding rate to find the overall reaction rate. The probability is estimated using at least 10^4 successful trajectories for each case.

Toehold length	$k_{\text{eff}}^{\text{AEL}}$ (/M/s)	$k_{\text{eff}}^{\text{expt}}$ (/M/s)
0	1.4	1.4
1	12	8.2
2	214	144
3	3.7×10^3	1.1×10^3
4	6.2×10^4	5.1×10^4
5	6.7×10^5	9.6×10^5
6	1.7×10^6	2.4×10^6
15	4.8×10^6	4.8×10^6

Table S1: Comparison of AEL predictions and experimental results from Zhang and Winfree (1) for the rate of displacement as a function of toehold length.

Performance of the AEL. Overall, these modifications to the IEL result in a self-consistent model with an initial binding rate that is linear in the length of the toehold. As with the IEL, the AEL has free parameters k_{bi}, ΔG_s and ΔG_p, and the overall acceleration with increased toehold length is largely determined by $\Delta G_s + \Delta G_p$. We fix $\Delta G_p = 2.0$ kcal/mol in accordance with experiment (Figure 7 of the main text), and adjust k_{bi} and ΔG_s to fit the data of Zhang and Winfree (1). We find that $k_{\text{bi}} = 3.30 \times 10^5$/M/s and $\Delta G_s = 3.60$ kcal/mol (implying $k_{\text{uni}} = 8.17 \times 10^6$/s) give a good fit to experiment, as summarised in Table S1.

S4 Secondary structure kinetics model

Multistrand (9) essentially employs a Gillespie algorithm (8) for generating statistically correct trajectories of a stochastic Markov process. Code implementing the Multistrand model is available for public download (http://www.dna.caltech.edu/Multistrand/).

Choice and timing of next transition. Suppose the box is in state i. Then, the next state m is chosen randomly from the states j which are adjacent to i (i.e. they differ from i by only one base pair), weighted by the rate of transition to each.

$$\mathbb{P}(\text{state } m \text{ is chosen}) = \frac{k_{im}}{\sum_j k_{ij}} \tag{54}$$

The time taken for the transition from i to m to occur (Δt) is chosen randomly from an exponential distri-

bution with rate parameter λ, where λ is the total rate of transitioning from the current state i. That is,

$$\mathbb{P}(\text{time taken is } \Delta t) = \lambda e^{-\lambda \Delta t} \tag{55}$$

where $\lambda = \sum_j k_{ij}$.

First step mode. We will describe first step mode for a general reaction of the form:

$$A + B \xrightarrow{k_{\text{eff}}} C + D \tag{56}$$

For a strand displacement reaction, which involves intermediate steps, this model assumes a low-concentration regime where the bimolecular step occurs on a much longer timescale than the unimolecular steps; equation 56 may then be used to accurately capture the dynamics.

The first step simulation mode begins with the bimolecular join step where A and B collide and form a base pair. The secondary structures of A and B are obtained by Boltzmann sampling the non-pseudoknotted secondary structure space for each molecule. If the bimolecular reaction rates are slow enough for the reactants to be in equilibrium, this sampling is valid. Once the secondary structures of A and B have been sampled, one of the available join steps is chosen at random and the simulation proceeds. As more trajectories are run, different initial secondary structures for A and B and different join steps are explored.

Note that we are not directly simulating the bimolecular join steps, whose rates are proportional to the simulated concentration (and are hence much slower than the unimolecular steps). This allows Multistrand to focus on the trajectories where a collision does occur, rather than spending most of the time simulating unimolecular reactions while waiting for the rare bimolecular reaction.

As simulation of a trajectory proceeds, two distinct end states are tracked: the molecules falling apart into the reactants (one of the A + B configurations), or forming the products (one of the C + D configurations). Each trajectory simulated may be classified as one that failed (if the former happens) or one that reacted (if the latter happens).

Our simulations yield the following data: first passage times for trajectories that reacted ($\Delta t^i_{\text{react}}$), first passage times for trajectories that failed (Δt^i_{fail}), the number of trajectories that reacted (N_{react}) and failed (N_{fail}), and the estimated average rate of collision (k_{coll} in /M/s) of the reactants A and B. For each trajectory, the rate of collision is calculated as $N_{\text{first}} \times k_{\text{bi}} \times u$, where N_{first} is the number of possible first base pairs between the sampled secondary structures of A and B for that trajectory and u is the simulated concentration. k_{coll} is estimated as the mean of the rates of collision for the trajectories simulated.

The following model is used to analyze simulation data. We assume that molecules A and B collide to either form a reactive molecule that will yield the products C and D (in our case, successful displacement) or a nonreactive molecule that will fall apart into the reactants A and B in some time (in our case, unsuccessful displacement).

$$A + B \xrightarrow{k_1} AB \xrightarrow{k_2} C + D \tag{57}$$

$$\mathrm{A} + \mathrm{B} \underset{k_2'}{\overset{k_1'}{\rightleftharpoons}} \mathrm{AB}' \tag{58}$$

Our model (equations 57, 58) is fitted as follows.

$$k_1 = \frac{N_{\text{react}}}{N_{\text{react}} + N_{\text{fail}}} \times k_{\text{coll}} \tag{59}$$

$$k_1' = \frac{N_{\text{fail}}}{N_{\text{react}} + N_{\text{fail}}} \times k_{\text{coll}} \tag{60}$$

$$k_2 = \frac{1}{\mathrm{E}[\Delta t^i_{\text{react}}]} \tag{61}$$

$$k_2' = \frac{1}{\mathrm{E}[\Delta t^i_{\text{fail}}]} \tag{62}$$

Assuming equation 56 is valid, k_{eff} may be predicted (9) based on our model as follows.

$$k_{\text{eff}} = \frac{1}{\Delta t_{\text{correct}}} \times \frac{1}{u} \tag{63}$$

where $\Delta t_{\text{correct}}$ is the expected time taken for a successful reaction to occur. $\Delta t_{\text{correct}}$ is calculated from the expected time for a failed collision to fall apart into the reactants (Δt_{fail}), and the expected time for a reactive collision to produce the products (Δt_{react}). Δt_{fail} and Δt_{react} depend on the expected time for any collision to occur (Δt_{coll}). These quantities are calculated as follows.

$$\Delta t_{\text{correct}} = \Delta t_{\text{fail}} \times \frac{k_1'}{k_1} + \Delta t_{\text{react}} \tag{64}$$

$$\Delta t_{\text{fail}} = \Delta t_{\text{coll}} + \frac{1}{k_2'} \tag{65}$$

$$\Delta t_{\text{react}} = \Delta t_{\text{coll}} + \frac{1}{k_2} \tag{66}$$

$$\Delta t_{\text{coll}} = \frac{1}{(k_1 + k_1') \times u} \tag{67}$$

In the low-concentration regime, the resolution of the three-stranded complex (resulting in successful displacement of the incumbent or dissociation of the invader) may be assumed to be effectively instantaneous compared to the rate of the bimolecular collision step. That is, we may assume $k_{\text{coll}} \times u << k_2, k_2'$.

Indeed, we make this assumption since we are inferring a bimolecular rate constant (equation 56). With that assumption, the general formulation (equation 63) may be reduced to

$$k_{\text{eff}} = k_{\text{coll}} \times p \tag{68}$$

where p is the probability that the collision results in successful displacement of the incumbent.

Simulation details. We simulated the "average strength toehold" experimental system of Zhang and Winfree (1), measuring strand displacement rates as a function of toehold length at 25 °C. We omitted the downstream step used for experimental detection purposes, and deleted the extra domain in the incumbent which was used only in that step. The sequences we used are provided in Table S2. Simulations were performed in first step mode.

Multistrand variations. The experimental system of Zhang and Winfree (1) employs a substrate strand with a 15-base overhang. Depending on the length of the invading toehold, a subset of this overhang is complementary to the toehold. The fact that the substrate overhang is longer than the toehold it binds to could conceivably have two effects: (i) stabilizing the first toehold base pair between the invader and the substrate through a dangle free energy contribution and/or (ii) allowing unexpected pathways of displacement through a larger set of possible first base pairs. Multistrand simulations with a matching length substrate overhang (truncated to match the length of the invading toehold) are closer to experiment by only 0.6 orders of magnitude (Figure S6(A)). This suggests that possible effects (i) and (ii) are not large enough to explain the discrepancy between Multistrand predictions and experimental measurements of strand displacement kinetics.

Because the energy models used by Multistrand (9), NUPACK (11), Mfold (13), and Vienna RNA (14) do not have a consensus method for handling dangle energy terms, we ran Multistrand simulations with each of the three options (Figure S6(A)). For each dangles option, k_{bi} and k_{uni} were separately calibrated to the same data (hybridization, zippering) used for calibrating the Metropolis method, as described in Schaeffer (9). Only minor differences were observed.

We also performed Multistrand simulations using the Kawasaki (3) method for assigning unimolecular transition rates, for which k_{bi} and k_{uni} were also recalibrated; again this yielded nearly identical results (Figure S6(B)).

Dependence on the ratio $\mathbf{k_{uni}/k_{bi}}$. When the invader is bound to the substrate by just one base of the toehold, it can either dissociate, leading to unsuccessful displacement, or form another base pair of the toehold and proceed towards zippering. Since dissociation is a bimolecular process, its rate is influenced by k_{bi}, while the rate of the unimolecular zippering process is influenced by k_{uni}. Decreasing $k_{\text{uni}}/k_{\text{bi}}$ increases the rate of the former relative to the latter. Although this is true for both short and long toeholds, short toeholds reach the state where the invader is bound to the substrate by just one base more often than long toeholds. So, decreasing $k_{\text{uni}}/k_{\text{bi}}$ disproportionately reduces the displacement rate of short toeholds and increases the orders of magnitude acceleration due to toehold length predicted by Multistrand (Figure S7).

S5 Measuring relative stability of strand displacement intermediates

DNA sequence design. DNA oligonucleotide sequences were designed by modifying sequences from Zhang and Winfree (1) by hand to get orthogonal domains `d` and `e`. Secondary structures of oligonucleotides and complexes were verified using the NUPACK web server (11) to be as intended.

Buffer conditions. DNA oligonucleotides were stored at 4 °C in TE buffer (10 mM Tris.HCl pH balanced to 8.0, with 1 mM EDTA.Na_2, purchased as 100x stock from Sigma-Aldrich). Prior to experimentation, TE buffer containing 62.5 mM $MgCl_2$ was added at a ratio of 1:4 to the sample, resulting in a final $MgCl_2$ concentration of 12.5 mM, out of which 1 mM is bound to EDTA. This buffer was used to prepare and store all oligonucleotide complexes, and to conduct all temperature dependent absorbance experiments, and will be referred to as "TE/Mg^{2+}" buffer.

Annealing and purification of complexes. All DNA oligonucleotides were purchased from Integrated DNA Technologies (IDT). Oligonucleotides of length 60 bases or less were ordered with HPLC purification, while those longer than 60 bases were ordered with IE-HPLC purification. Concentrations were estimated from absorbance at 260 nm (measured using a Thermo Scientific NanoDrop cuvette-free spectrophotometer) using calculated extinction coefficients (15).

All complexes `Xi:Yj` were prepared by annealing `Xi` (at an approximate concentration of 25 μM) with `Yj` (at 20% excess) in TE/Mg^{2+} buffer. All annealing operations were performed in an Eppendorf Mastercycler Gradient thermocycler. The samples were cooled at a constant rate from 95 °C to 20 °C in 90 min.

All complexes were purified by nondenaturing

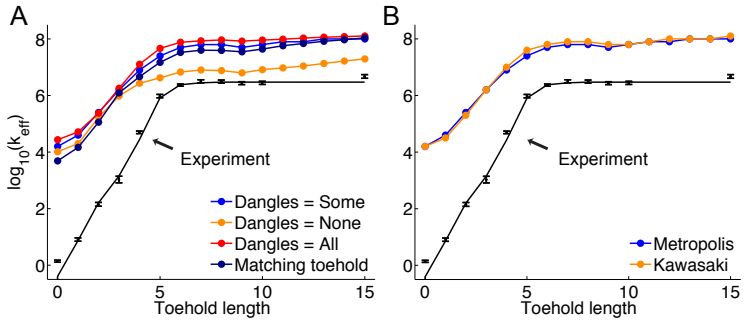

Figure S6: Multistrand simulations at 25 °C with different choices: (A) (i) in treating free energy contributions due to dangles (10) (options "Some"(default), "None" and "All" in the NUPACK (11) energy model (12)) and (ii) with substrate overhangs only as long as the toehold on the invader - i.e. matching length bottom toeholds on the substrate, rather than the full 15 base overhang used by Zhang and Winfree (1) (B) different ways of assigning absolute transition rates for unimolecular steps while satisfying detailed balance. Note that none of the variations are able to account for the experimental data points (in black) from Zhang and Winfree (1); solid black line is their phenomenological model. Standard errors for Multistrand simulations are under 1% (not shown).

Strand	Sequence
Substrate	5′- *GAAGTGACATGGAGA* CGTAGGGTATTGAATGAGGG -3′
Incumbent	5′- CCCTCATTCAATACCCTACG -3′
Invader	5′- CCCTCATTCAATACCCTACG *TCTCCATGTCACTTC* -3′

Table S2: Sequences used in Multistrand simulations of strand displacement, with toeholds in italics. For toehold lengths less than 15, the toehold of the invader is truncated to the appropriate length, measured from the 5' end. For simulations with a matching length substrate overhang, the toehold of the substrate was also truncated to match the toehold of the invader.

(ND) polyacrylamide gel electrophoresis (PAGE) by running the samples on 12% gel at 150 V for approximately 6h. The acrylamide (19:1 acrylamide:bis) was diluted from 40% acrylamide stock purchased from Ambion. ND loading dye containing xylene cyanol FF in 50% glycerol was added to all samples, resulting in a final gycerol concentration of 10% by volume. The appropriate bands were cut out and eluted in 1 mL of TE/Mg^{2+} buffer for 2 days. Purified complexes were quantitated from absorbance at 260 nm (measured using a Thermo Scientific NanoDrop cuvette-free spectrophotometer) using calculated extinction coefficients (15). Typical yields ranged from 40% to 60%.

Temperature-dependent absorbance experiment protocols. Temperature-dependent absorbance experiments were performed using a Model 14 UV-Vis spectrophotometer, equipped with a water bath temperature controller, from AVIV Biomedical, Lakewood, NJ. UV absorbance at 260 nm between 20 °C and 90 °C was measured with a 1 nm bandwidth using 1.6 mL quartz cuvettes. The temperature step was set at 0.1 °C/min with a 0.1 °C deadband and an equilibration time of 0.25 minutes. All cuvettes were thoroughly cleaned before each experiment: each cuvette was washed 15 times in distilled water, once in 70% ethanol, another five times in distilled water, and finally once more in 70% ethanol.

One temperature-dependent absorbance experiment consisted of: (i) heating from 20 °C to 90 °C, before taking any measurements; (ii) annealing from 90 °C to 20 °C while measuring absorbance every 0.1 °C; (iii) holding for 2h at 20 °C; (iv) melting from 20 °C to 90 °C while measuring absorbance every 0.1 °C. All heating and annealing steps in an experiment were at the temperature step mentioned above (0.1 °C/min). An example of raw temperature-dependent absorbance data at 200 nM obtained while annealing (step ii) is provided in Figure S8.

For each complex, one sample was prepared at each of four different concentrations. For each of those samples, two runs of the temperature-dependent absorbance experiment described above were performed.

Two state model. We analyze the temperature-dependent absorbance data using a two-state model (16): each molecule is assumed to be either in the fully bound state (`Xi:Yj`) or the fully dissociated state (`Xi + Yj`).

The raw absorbance data was smoothed by a moving average of 30 points (corresponding to a temperature interval of 3 °C). The "melt fraction" or fraction of complex dissociated at temperature T ($f(T)$) was calculated by normalizing the average absorbance of the bound state (between [20 °C, 35 °C]) to 0 and that of the dissociated state (between a concentration-dependent upper normalization range - see Table S3) to 1. Note that the upper normaliza-

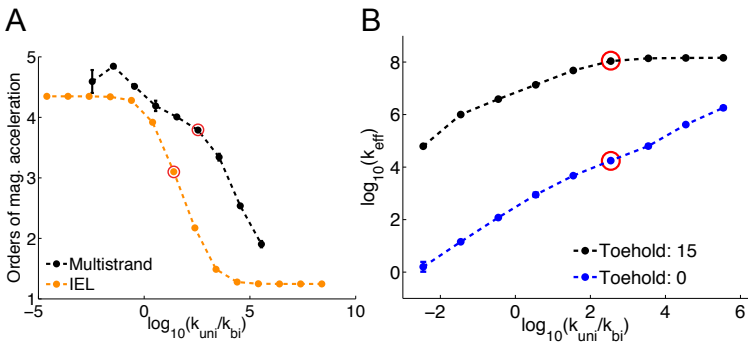

Figure S7: The dependence of Multistrand predictions on $k_{\text{uni}}/k_{\text{bi}}$ (red circles indicate default value of $k_{\text{uni}}/k_{\text{bi}}$). Error bars are 3∗SE long where SE is the standard error. (A) Orders of magnitude acceleration in k_{eff} between toehold lengths 15 and 0 ($\mathcal{A}_{15,0}$), as predicted by Multistrand, as a function of $\log_{10}(k_{\text{uni}}/k_{\text{bi}})$. IEL(2.6, 0) predictions are shown for comparison. Even implausibly low values of $k_{\text{uni}}/k_{\text{bi}}$ do not result in acceleration that matches the experimentally observed value of 6.5 orders of magnitude. (B) $\log_{10}(k_{\text{eff}})$ vs $\log_{10}(k_{\text{uni}}/k_{\text{bi}})$ for toehold lengths 15 and 0. The surprising non-monotonicity in (A) at the lowest value of $k_{\text{uni}}/k_{\text{bi}}$ is observed to arise from the disproportionately large decrease in $\log_{10}(k_{\text{eff}})$ for toehold length 15 in (B). We hypothesize that this is likely a sequence dependent effect.

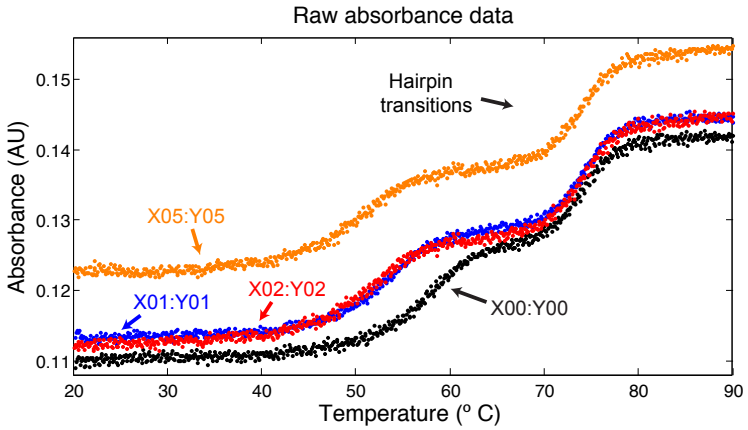

Figure S8: Raw absorbance data (at 260 nm), while annealing, at a concentration of 200 nM. Measurements were taken every 0.1 °C between 20 °C and 90 °C. The lower temperature transition is the (bimolecular) formation of the complex, while the higher temperature transition is the (unimolecular) formation of the hairpin. Data acquired by annealing and melting are essentially superimposable.

tion range at a given concentration is the same for all complexes. Our results are robust to the choice of upper normalization range; this was verified by repeating the analysis with $[65, 67]$ °C as the upper normalization range across all concentrations.

Given the initial concentration c of the complex `Xi:Yj`, the melt fraction $f(T)$ at temperature T in the two-state model can be calculated from $(\Delta H^\circ, \Delta S^\circ)$ as follows. Consider the reaction `Xi + Yj` $\rightleftarrows$ `Xi:Yj`, at temperature T. Let us assume that the initial concentration c of `Xi:Yj` dissociates to `Xi` and `Yj` at concentration x each. Then, `Xi:Yj` is at concentration $c - x$. We know that the equilibrium constant $K_{\text{eq}}(T)$ is related to $f(T)$ as

$$K_{\text{eq}}(T) = \frac{c - x}{x^2} = \frac{1 - f(T)}{c f(T)^2} \tag{69}$$

Solving the quadratic equation for $f(T) \geq 0$, we get

$$f(T) = \frac{-1 + \sqrt{1 + 4cK_{\text{eq}}(T)}}{2cK_{\text{eq}}(T)} \tag{70}$$

Since $K_{\text{eq}}(T) = \exp(-\frac{\Delta G^\circ(T)}{RT})$, we may predict the entire temperature-dependent melt fraction curve by varying T appropriately.

For each complex, we infer $(\Delta H^\circ, \Delta S^\circ)$ (and hence ΔG°_{25}, ΔG°_{55}) by fitting the predicted melt fraction curves to smoothed and normalized absorbance data across different concentrations. By comparing the free energies of different complexes, we can infer the contribution of the poly-`T` overhangs. We do this in two ways: a Bayesian analysis and a descriptive "leave-one-concentration-out" fit.

Bayesian analysis. We essentially discretize the $(\Delta H^\circ, \Delta S^\circ)$ space into a grid and calculate the likelihood that our experimental data for each complex

Concentration (nM)	Upper normalization range (°C)
100	[61, 63]
150	[63, 65]
200	[64, 66]
300	[65, 67]
400	[65, 67]
500	[65, 67]

Table S3: Melt fraction for each complex is calculated from smoothed absorbance data by normalizing the absorbance in the [20, 35] °C range to 0 and the absorbance in the concentration-dependent upper normalization range, specified in this Table, to 1. Our results are robust to this choice; this was verified by repeating the analysis with [65, 67] °C as the upper normalization range across all concentrations.

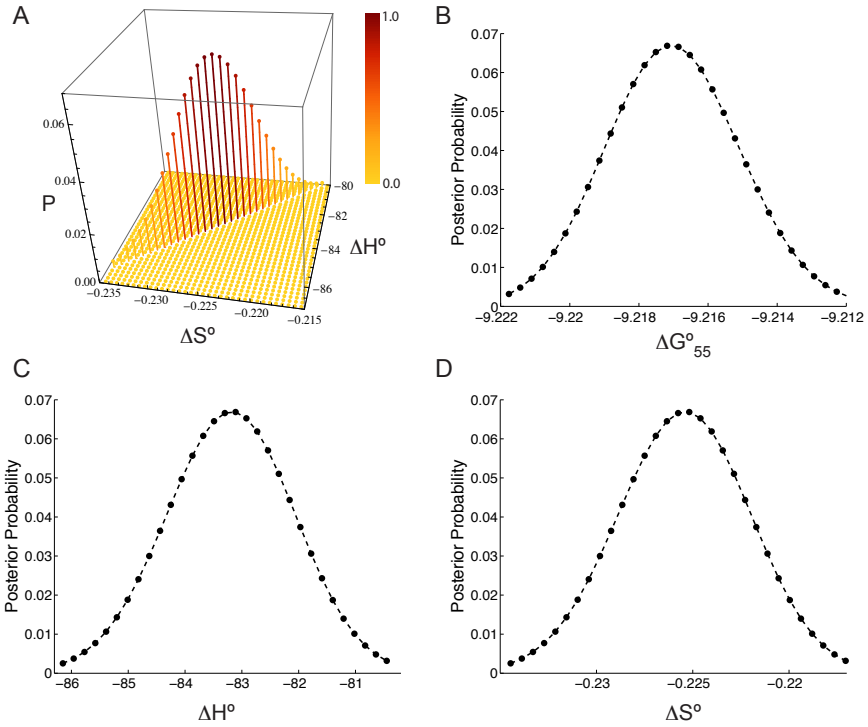

Figure S9: Example posterior probability distributions obtained by Bayesian analysis over (A) $(\Delta H^\circ, \Delta S^\circ)$ space and marginals over (B) ΔG° at 55 °C, (C) ΔH° and (D) ΔS° for complex `X10:Y10`. All ΔG°_{55} and ΔH° values are in kcal/mol while ΔS° values are in kcal/K/mol. Note that the 99% confidence interval is much more narrow for ΔG°_{55} compared to ΔH° and ΔS°.

(all data traces at four concentrations) arose from each candidate pair in the discretization, assuming an independent Gaussian noise model. Normalizing the likelihood yields the posterior distribution for ΔH°, ΔS° and ΔG° (e.g. Figure S9). We calculate posterior means and 99% confidence intervals, under the assumptions of the two-state model and our Bayesian framework.

In other words, given candidate values of the standard enthalpy and entropy of formation, $(\Delta H_0^\circ, \Delta S_0^\circ)$, for a particular complex, smoothed and normalized absorbance data D_{T_i,c_j} at a certain temperature T_i and concentration c_j is assumed to be related to the predicted melt fraction f_{T_i,c_j} as follows:

$$D_{T_i,c_j} = f_{T_i,c_j} + \xi_{T_i,c_j} \tag{71}$$

where

$$\xi_{T_i,c_j} \sim \mathcal{N}(0, \sigma^2_{T_i,c_j})$$

is independent additive Gaussian noise. That is, ξ_{T_i,c_j} and ξ_{T_l,c_k} are assumed to be independent if $T_i \neq T_l$ or $c_j \neq c_k$. $\sigma^2_{T_i,c_j}$ is calculated as the sample variance of smoothed and normalized absorbance data points at concentration c_j in a neighborhood around T_i (three points on either side of T_i).

With these assumptions, the likelihood of observing the data given the estimate $(\Delta H_0^\circ, \Delta S_0^\circ)$ is simply

$$L(\Delta H_0^\circ, \Delta S_0^\circ) = \prod_{T_i,c_j} \phi_{f_{T_i,c_j},\sigma^2_{T_i,c_j}}(D_{T_i,c_j}) \tag{72}$$

where ϕ_{μ,σ^2} is the probability density function of the Gaussian distribution with mean μ and variance σ^2.

Starting with a uniform prior over the $(\Delta H^\circ, \Delta S^\circ)$ grid, the posterior probability distribution is proportional to the likelihood (this standard result from Bayesian statistics is justified later). So, normalizing the likelihood of observing our data, we can calculate the posterior distribution:

$$P(\Delta H_0^\circ, \Delta S_0^\circ) = \frac{L(\Delta H_0^\circ, \Delta S_0^\circ)}{\sum_{\Delta H_i^\circ, \Delta S_j^\circ} L(\Delta H_i^\circ, \Delta S_j^\circ)} \tag{73}$$

In practice, we first perform a coarse discretization of $(\Delta H^\circ, \Delta S^\circ)$ space in order to identify the region containing non-zero values of the posterior probability; we then perform a fine discretization of that region and evaluate the posterior probability over it.

Once we have the posterior probability over $(\Delta H^\circ, \Delta S^\circ)$ space, we find the smallest region containing 99% of the probability, and then evaluate marginal posterior probability distributions for ΔH°, ΔS°, ΔG°_{25} and ΔG°_{55} (Figure S9). The 99% confidence intervals are relatively much narrower for ΔG°_{55} than ΔH° or ΔS°. This shows that our data permits accurate comparison of the stability of our complexes through ΔG°, but cannot easily separate the enthalpic and entropic contributions. Also note that error bars and 99% confidence intervals are much narrower for ΔG°_{55} (Figure S10) compared to ΔG°_{25} (Figure 8 in the main text). This is to be expected because the former temperature is closer to the experimental melting temperature of our complexes. With the assumptions in the two-state model and our Bayesian framework, we report posterior means and 99% confidence intervals for quantities of interest (Table S5, Figure S10).

Relationship between posterior probability and likelihood. We now recall that with a uniform prior, the posterior probability distribution is proportional to the likelihood. For a more detailed introduction, see Gelman et al. (17). Suppose θ is a vector of parameters we want to infer, and that we have data $\mathcal{D}$ which is informative about θ. Then, we know

$$\mathbb{P}(\theta, \mathcal{D}) = \mathbb{P}(\theta) \times \mathbb{P}(\mathcal{D}|\theta) = \mathbb{P}(\mathcal{D}) \times \mathbb{P}(\theta|\mathcal{D}) \tag{74}$$

Therefore the posterior distribution $\mathbb{P}(\theta|\mathcal{D})$ is obtained by

$$\mathbb{P}(\theta|\mathcal{D}) = \frac{\mathbb{P}(\theta) \times \mathbb{P}(\mathcal{D}|\theta)}{\mathbb{P}(\mathcal{D})} \tag{75}$$

Here, $\mathbb{P}(\theta)$ is constant because we start with a uniform prior. $\mathbb{P}(\mathcal{D}) = \sum_\theta \mathbb{P}(\theta) \times \mathbb{P}(\mathcal{D}|\theta)$ is also independent of θ. $\mathbb{P}(\mathcal{D}|\theta)$ is nothing but the likelihood. Hence, with a uniform prior, the posterior distribution is proportional to the likelihood.

Leave-one-concentration-out analysis. This is a simple and descriptive way of analyzing the data, which essentially serves as a sanity check. Data from each complex is analyzed separately to infer the free energy of formation of that complex. We measured temperature-dependent absorbance data at four concentrations. Here, we sequentially leave out data from one concentration at a time, thus generating four datasets, each containing data from three concentrations. For each dataset, we perform a simultaneous nonlinear least squares fit (using the Levenberg-Marquardt algorithm, implemented by a built-in MATLAB function) of the predicted melt fraction curves to the smoothed and normalized absorbance data across all three concentrations present in the dataset. This procedure generates four estimates of $(\Delta H^\circ, \Delta S^\circ)$ of formation for each complex, one for each leave-one-concentration-out dataset. We then calculate ΔG°_{25} and ΔG°_{55} for each of those four

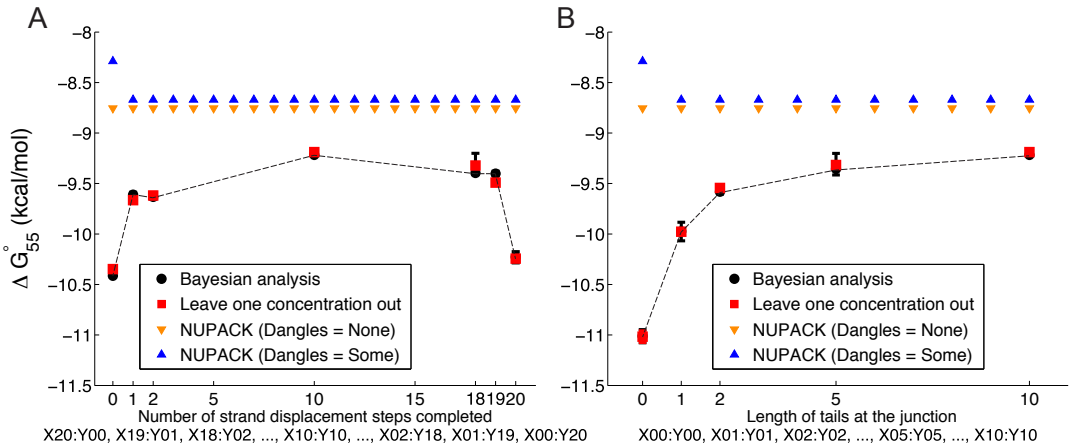

Figure S10: ΔG° of formation (at 55 °C) of complexes in the *strand displacement snapshot* study (A) or the *local overhang* study (B). Error bars in black indicate Bayesian posterior means and 99% confidence intervals. Error bars in red indicate means and standard deviations of leave-one-concentration-out least square fits. NUPACK predictions with dangles options "some" and "none" are provided for comparison.

Complex	$\Delta G^\circ_{25,\ avg}$	$\Delta G^\circ_{25,\ sd}$	$\Delta G^\circ_{55,\ avg}$	$\Delta G^\circ_{55,\ sd}$
X20:Y00	-18.00	0.15	-10.35	0.023
X19:Y01	-16.48	0.14	-9.66	0.013
X18:Y02	-16.15	0.11	-9.62	0.031
X10:Y10	-16.03	0.14	-9.19	0.033
X02:Y18	-16.36	0.08	-9.32	0.029
X01:Y19	-16.44	0.16	-9.49	0.014
X00:Y20	-17.96	0.09	-10.24	0.027
X00:Y00	-19.17	0.31	-11.02	0.058
X01:Y01	-17.78	0.06	-9.98	0.017
X02:Y02	-16.92	0.27	-9.54	0.008
X05:Y05	-16.22	0.28	-9.32	0.028

Table S4: Leave-one-concentration-out mean and standard deviation for ΔG° at 25 °C and 55 °C, for each complex. All values in kcal/mol.

Complex	E[ΔH°]	ΔH°_{CI}	E[ΔS°]	ΔS°_{CI}	E[ΔG°_{25}]	$\Delta G^\circ_{25,\ CI}$
X20:Y00	-93.2	[-97.8, -88.8]	-0.252	[-0.266, -0.239]	-17.99	[-18.42, -17.56]
X19:Y01	-84.9	[-89.1, -81.0]	-0.229	[-0.242, -0.217]	-16.49	[-16.85, -16.16]
X18:Y02	-80.9	[-84.8, -77.3]	-0.217	[-0.229, -0.206]	-16.15	[-16.49, -15.84]
X10:Y10	-83.2	[-86.2, -80.4]	-0.226	[-0.234, -0.217]	-15.98	[-16.25, -15.73]
X02:Y18	-83.9	[-92.8, -80.1]	-0.227	[-0.255, -0.215]	-16.21	[-16.84, -15.87]
X01:Y19	-87.5	[-91.6, -83.5]	-0.238	[-0.250, -0.226]	-16.54	[-16.99, -16.19]
X00:Y20	-97.0	[-99.8, -89.8]	-0.264	[-0.273, -0.242]	-18.16	[-18.47, -17.54]
X00:Y00	-100.3	[-104.6, -96.2]	-0.272	[-0.285, -0.260]	-19.18	[-19.63, -18.74]
X01:Y01	-95.8	[-103.5, -88.1]	-0.262	[-0.285, -0.238]	-17.82	[-18.49, -17.16]
X02:Y02	-89.9	[-94.3, -85.6]	-0.245	[-0.258, -0.232]	-16.92	[-17.30, -16.55]
X05:Y05	-83.9	[-92.0, -78.7]	-0.227	[-0.252, -0.211]	-16.17	[-16.78, -15.75]

Table S5: Bayesian posterior means and 99% confidence intervals for ΔH°, ΔS° and ΔG°_{25} for each complex. ΔH° and ΔG°_{25} values are in kcal/mol while ΔS° is in kcal/K/mol.

estimates and report the mean and standard deviation, for each complex (Table S4).

S6 Coarse-grained molecular modeling

A Coarse-grained molecular model. OxDNA and its interaction potentials have been described in detail by Ouldridge. (18) Code implementing OxDNA is available for public download (http://dna.physics.ox.ac.uk/). OxDNA represents DNA as a string of nucleotides, where each nucleotide (sugar, phosphate and base group) is a rigid body with interaction sites for backbone, stacking and hydrogen-bonding interactions. The potential energy of the system can be decomposed as

$$V = \sum_{\langle ij \rangle} \left(V_{\text{b.b.}} + V_{\text{stack}} + V_{\text{exc}}^{'} \right) + \sum_{i,j \notin \langle ij \rangle} \left(V_{\text{HB}} + V_{\text{cr.st.}} + V_{\text{exc}} + V_{\text{cx.st.}} \right), \quad (76)$$

where the first sum is taken over all nucleotides that are nearest neighbors on the same strand and the second sum comprises all remaining pairs. The interactions between nucleotides are schematically shown in Figure S11. The backbone potential $V_{\text{b.b.}}$ is an isotropic spring that imposes a finite maximum distance between backbone sites of neighbours, mimicking the covalent bonds along the strand. The hydrogen bonding (V_{HB}), cross stacking ($V_{\text{cr.st.}}$), coaxial stacking ($V_{\text{cx.st.}}$) and stacking interactions (V_{stack}) are anisotropic and explicitly depend on the relative orientations of the nucleotides as well as the distance between the relevant interaction sites. This orientational dependence captures the planarity of bases, and drives the formation of helical duplexes. The coaxial stacking term is designed to capture stacking interactions between bases that are not immediate neighbours along the backbone of a strand. Bases and backbones also have excluded volume interactions V_{exc} or $V_{\text{exc}}^{'}$.

Hydrogen-bonding interactions are only possible between complementary (A-T and C-G) basepairs, but no other sequence-dependence is included in oxDNA. Consequently, the interactions were fitted to reproduce melting temperatures of 'average' oligonucleotides, obtained by averaging over the parameters of SantaLucia's nearest-neighbour model (19), and the structural and mechanical properties of double- and single-stranded DNA.

oxDNA does not have any explicit electrostatic interactions. It was fitted to reproduce DNA behavior at salt concentration $[\text{Na}^+] = 0.5\text{M}$, where the electrostatic properties are strongly screened, and it may be reasonable to incorporate them into a short-ranged excluded volume. Possible issues related to salt concentrations are discussed in the main text. It should be noted that the oxDNA neglects several features of the DNA structure and interactions due to the high level of coarse-graining. Specifically, the double helix in the model is symmetrical rather than the grooves between the backbone sites having different sizes (i.e., major and minor grooving), and all four nucleotides have the same structure.

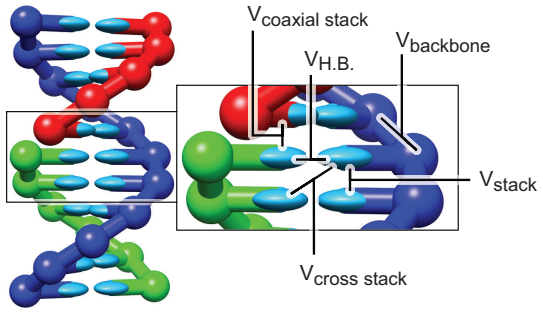

Figure S11: A model DNA duplex, with stabilising interactions depicted schematically. The backbone sites are shown as spheres, the bases as ellipsoids. Backbone colouring indicates strand identity. All nucleotides also interact with repulsive excluded volume interactions. The coaxial stacking interaction acts like a stacking interaction between bases that are not immediate neighbours along the backbone of a strand.

Simulation Techniques. The thermodynamic properties of the molecular model are obtained by averaging over the Boltzmann distribution

$$\rho(\mathbf{r}^N, \mathbf{p}^N, \mathbf{q}^N, \mathbf{L}^N) \propto \mathrm{e}^{(-\beta \mathcal{H}(\mathbf{r}^N, \mathbf{p}^N, \mathbf{q}^N, \mathbf{L}^N))}. \quad (77)$$

Here $\mathcal{H}$ is the system Hamiltonian, which is a function of positional and angular particle coordinates $\mathbf{r}^N$ and $\mathbf{q}^N$ and their generalized momenta $\mathbf{p}^N$ and $\mathbf{L}^N$. As the terms containing $\mathbf{p}^N$ and $\mathbf{L}^N$ in $\mathcal{H}$ are separable and can be analytically integrated out, the probability of a certain configuration is proportional to a Boltzmann factor for its potential energy, $\exp(-\beta V(\mathbf{r}^N, \mathbf{q}^N))$. Obtaining kinetic properties requires an additional choice of dynamics. The Virtual Move Monte Carlo (VMMC), and Langevin Dynamics (LD) algorithms used for thermodynamic and kinetic properties respectively are outlined in the following sections.

Virtual Move Monte Carlo. Monte Carlo techniques involve randomly generating trial moves of a system consisting of a set of particles, and accepting those moves with probabilities that ensure the simulation samples from the distribution given in equation 77. The widely used Metropolis Monte Carlo algorithm (MMC) (4) attempts random moves of single

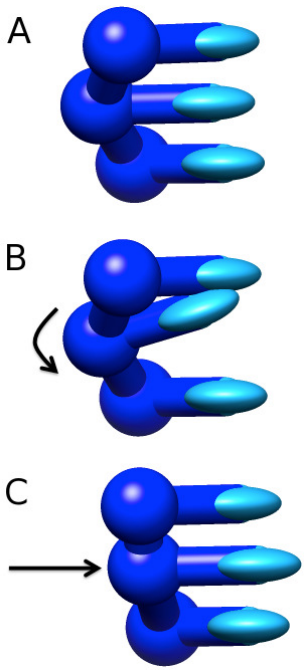

Figure S12: Examples of initial 'single particle' seed moves attempted in our implementation of the VMMC algorithm. (A) Initial state. (B) New state obtained from (A) after rotating the central nucleotide about its backbone site. (C) New state obtained from (A) after translating the central nucleotide. In each of the new states, the flanking nucleotides act as a reference: they have exactly the same position and orientation as in (A). Once an initial 'seed' move such as (B) or (C) has been selected, clusters are grown from this seed in the manner outlined by Whitelam *et al.* (20)

particles, and accepts those moves with a probability

$$P_{\text{acc}}(\mu \to \nu) = \min\{1, \exp\left(-\beta(V^{\nu} - V^{\mu})\right)\}, \quad (78)$$

where μ and ν represent initial and final states respectively. Although simple to implement, MMC can struggle to equilibrate strongly interacting systems as moves of single particles tend to generate large increases in energy, and are therefore rejected.

The VMMC algorithm (21, 20) overcomes this problem by generating clusters that depend on energy changes resulting from attempted moves (we use the variant presented in the appendix of Whitelam *et al.* (20)). A random single particle move is chosen, and energy changes due to that move are calculated with all neighbours of the seed particle. Those particles for which the energy is increased are probabilistically added to the cluster, and move together with the seed particle. The process is then repeated with neighbours of the newly added particles, until no more new links are formed. Due to the statistical biases introduced during cluster building, a more complex acceptance factor than equation 78 is required in order to satisfy detailed balance.

In the context of the molecular model studied in this work, a 'single particle' is a nucleotide, and the attempted moves are translation of a whole nucleotide and rotation of a nucleotide about its backbone site. These moves are illustrated in Figure S12.

Umbrella sampling. Despite the efficiency of VMMC, obtaining accurate statistics for the free-energy landscape of displacement and the stability of a duplex can be difficult. Equilibration can be accelerated by flattening free-energy barriers with an artificial biasing weight $W(\mathbf{r}^N, \mathbf{q}^N)$ (22). A lower barrier means transitions occur more quickly, and equilibration is accelerated. The thermodynamic expectation of any variable A follows from the biased sample obtained as

$$\begin{aligned}\langle A\rangle &= \frac{\int \mathrm{d}\mathbf{r}^N \mathrm{d}\mathbf{q}^N A(\mathbf{r}^N,\mathbf{q}^N)\mathrm{e}^{-\beta V(\mathbf{r}^N,\mathbf{q}^N)}}{\int \mathrm{d}\mathbf{r}^N \mathrm{d}\mathbf{q}^N \mathrm{e}^{-\beta V(\mathbf{r}^N,\mathbf{q}^N)}} \\ &= \frac{\int \mathrm{d}\mathbf{r}^N \mathrm{d}\mathbf{q}^N \frac{A(\mathbf{r}^N,\mathbf{q}^N)}{W(\mathbf{r}^N,\mathbf{q}^N)} W(\mathbf{r}^N,\mathbf{q}^N)\mathrm{e}^{-\beta V(\mathbf{r}^N,\mathbf{q}^N)}}{\int \mathrm{d}\mathbf{r}^N \mathrm{d}\mathbf{q}^N \frac{1}{W(\mathbf{r}^N,\mathbf{q}^N)} W(\mathbf{r}^N,\mathbf{q}^N)\mathrm{e}^{-\beta V(\mathbf{r}^N,\mathbf{q}^N)}} \\ &= \frac{\langle A(\mathbf{r}^N,\mathbf{q}^N)/W(\mathbf{r}^N,\mathbf{q}^N)\rangle_W}{\langle 1/W(\mathbf{r}^N,\mathbf{q}^N)\rangle_W}. \end{aligned} \quad (79)$$

Here $\langle\rangle_W$ indicates the expectation found by sampling from the biased distribution $W(\mathbf{r}^N, \mathbf{q}^N)\exp(-\beta V(\mathbf{r}^N, \mathbf{q}^N))$. For simulations in this paper an initial $W(\mathbf{r}^N, \mathbf{q}^N)$ was chosen from experience, and improved by hand as required.

Langevin Dynamics. Langevin Dynamics is an approach for generating diffusive motion of coarse-grained models with implicit solvent. The principle is that the solvent exerts both random forces and dissipative drag on the solute, and that the two are related by a fluctuation-dissipation relation to ensure that the steady-state distribution is given by equation 77. Newton's equations, with the addition of these solvent-mediated forces, can then be integrated to give dynamical trajectories. In this work, we use the quaternion-based algorithm of Davidchack *et al.* (23) as an efficient methodology for simulating rigid bodies.

To use this algorithm, it is necessary to specify a friction tensor relating the drag forces experienced by a particle to its momenta. For simplicity, we assume each nucleotide interacts with the solvent in a spherically symmetric manner, meaning that the task is reduced to identifying linear and rotational damping coefficients, γ and Γ. We choose values of $\gamma = 0.59\,\mathrm{ps}^{-1}$ and $\Gamma = 1.76\,\mathrm{ps}^{-1}$. These values are around one to two orders of magnitude smaller than would be inferred for a objects the size of nucleotides in a fluid with the viscosity of water. Lower friction coefficients accelerate dynamics, which would

have been prohibitively slow otherwise, but still reproduce diffusive motion. It is reasonable to assume that, for the comparison of relative rates of similar processes, this choice will not be overly important given the number of approximations already inherent in the oxDNA. Indeed, simulations with $\gamma = 5.9\,\mathrm{ps}^{-1}$ and $\Gamma = 17.6\,\mathrm{ps}^{-1}$ showed no measurable difference in the probability of successful displacement for a 3-base toehold once attached. Furthermore, the sequence of states visited during unbiased VMMC simulations provides another (less rigorous) approximation to dynamics. These simulations give a somewhat lower success rate of displacement from a toehold-bound state than LD. The net effect, however, is simply a shifting of the start of the plateau by around half a base pair, and the qualitative arguments are still valid. These results suggest the findings presented here are not strongly sensitive to the choice of dynamics. Simulations reported in this work were performed with a time step of 5.13 fs. As shown by Ouldridge (18), such a time step reproduces the average energies of a duplex and the hairpin-folding kinetics obtained with much smaller integration time steps.

Forward flux sampling. Forward flux sampling (FFS) allows the calculation of the flux between two local minima of free energy, and also sampling from the ensemble of trajectories that link the two minima (24, 25). The term 'flux' from (meta)stable state A to state B has the following definition.

> Given an infinitely long simulation in which many transitions are observed, the flux of trajectories from A to B is $\Phi_{AB} = N_{AB}/(\tau f_A)$, where N_{AB} is the number of times the simulation leaves A and then reaches B, τ is the total time simulated and f_A is the fraction of the total time simulated for which state A has been more recently visited than state B.

The concept of flux is therefore a generalization of a transition rate for processes that are not instantaneous: it incorporates the time spent in intermediate states between A and B. In our simulations of displacement, state A is the initial configuration of incumbent bound to substrate, with invading strand unattached, and B is the state with the invading strand bound to the substrate with the incumbent strand unattached. The three-stranded complexes involved in branch migration are intermediate states.

In the experimental work of Zhang and Winfree (1), bimolecular rate constants for strand displacement

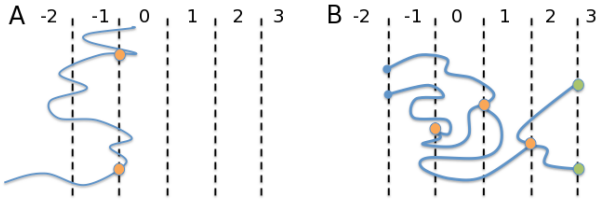

Figure S13: Schematic illustration of FFS. The space is divided into different values of the order parameter Q by interfaces, with Q values indicated by numbers in the figure. We wish to estimate the flux from $Q = -2$ to $Q = Q_{\max} = 3$. (A) First stage, estimating the flux across the interface λ^0_{-1} between $Q = -1$ and $Q = 0$. Circles indicate crossings of the interface that contribute to the flux; only positive crossings are counted, and only the first crossing since leaving $Q = -2$. (B) Subsequent stages, estimating the probability of reaching interface λ^Q_{Q-1} from λ^{Q-2}_{Q-1}. In this example, two trajectories are launched from each point at the prior interface. These trajectories end either by successfully reaching λ^Q_{Q-1} , or by failing and returning to λ^{-1}_{-2}.

are measured using bulk systems at low concentrations ($\sim$ nM). In our simulations, we use three strands in a periodic cell of volume 1.67×10^{-20} L. The periodic boundary conditions allow us to mimic a bulk system, and the volume used corresponds to a concentration of approximately 100 µM for each strand. If the simulation time spent in intermediate states were negligible, fluxes could then be taken directly as instantaneous reaction rates, allowing bimolecular rate constants to be inferred and compared to experiments. At such a high concentration as 100 µM, however, we find that the time scale for resolving a three-stranded complex (when either displacement is completed, or the invading strand detaches) can be a significant contribution to the overall displacement reaction time. It is reasonable to assume that the time required to resolve the three-stranded complex does not scale with simulation concentration, and therefore should not contribute to rate constants at the low concentrations typical of experiment. To make a fair comparison to experiment, therefore, we must not include time spent in three-stranded complexes in our estimate of the flux. Mathematically, this corresponds to redefining f_A so that it doesn't include time spent in three-stranded intermediates. The measurements of flux thus recorded are reported in the main text as transition rates, as the assumption of instantaneous transitions for a dilute solution is implicit in the measurement process.

FFS is illustrated schematically in Figure S13. We first discuss FFS generally, before specifying the implementation for our system. We require an order parameter Q that measures the extent of the reaction, such that non-intersecting interfaces λ^Q_{Q-1} can be drawn between consecutive values of Q. We de-

fine the lowest value of Q as $Q = -2$ because the procedure for interfaces λ^Q_{Q-1} with $Q > 0$ is distinct from that for $Q \leq 0$. Initially, simulations are performed that begin in the lowest value of Q and the flux of trajectories crossing the surface λ^0_{-1} (for the first time since leaving $Q = -2$) is measured. Note that the simulation is not restarted when trajectories cross λ^0_{-1}.

The total flux of trajectories from $Q = -2$ to the alternative minima ($Q = Q_{\max}$) is then calculated as the flux across λ^0_{-1} from $Q = -2$, multiplied by the conditional probability that these trajectories reach $Q = Q_{\max}$ before returning to $Q = -2$, $P(\lambda^{Q_{\max}}_{Q_{\max}-1}|\lambda^0_{-1})$. This probability can be factorized into the product of the probabilities of trajectories starting from the interface λ^Q_{Q-1} reaching the interface λ^{Q+1}_Q before returning to $Q = -2$

$$P(\lambda^{Q_{\max}}_{Q_{\max}-1}|\lambda^0_{-1}) = \Pi^{Q_{\max}}_{Q=1} P(\lambda^Q_{Q-1}|\lambda^{Q-1}_{Q-2}). \quad (80)$$

The simulation then proceeds by randomly loading microstates which correspond to the crossing of λ^0_{-1}, and using these as initial points from which to estimate $P(\lambda^1_0|\lambda^0_{-1})$. The process is then iterated for successive interfaces, allowing the estimation of flux and the construction of trajectories sampled from the distribution of transition pathways.

Simulation implementation.

Kinetics of displacement. Three strands of DNA (substrate, incumbent and invading strand, with sequences as given in the Table S6) were simulated in a periodic cubic cell of 1.67×10^{-20} l, at a temperature of $T = 25°\mathrm{C}$, using the LD algorithm with FFS. Strands were initialized with the incumbent bound to the substrate and the invading strand separate, and equilibrated for 0.513 µs. Given the diffusion constant of model DNA ($\sim 10^{-9}\,\mathrm{m^2 s^{-1}}$ for our system with $\gamma = 0.59\,\mathrm{ps^{-1}}$ and $\Gamma = 1.76\,\mathrm{ps^{-1}}$), this is approximately the time required for the reactant DNA molecules to diffuse by the length of the simulation cell. It is also far longer than the decorrelation time of the potential energy of the reactants (around 1 ns).

To simplify the sampling, we used an approach in which only the expected base pairs between the incumbent and the substrate or the invading strand and the substrate are given non-zero binding strength - we shall refer to these base pairs as *correct base pairs*. In a full system, incorrect base pairs can potentially contribute to association processes, typically through the formation of metastable misbonded structures that then relax into the intended configuration (26). The metastability of these misbonded structures would make them difficult to incorporate into the FFS simulations of displacement. As the sequences used by Zhang and Winfree (1) were deliberately designed to minimize the occurrence of misbonded configurations, we expect that this simplification should have minor systematic effects on our measurements. We also tested this assumption by measuring the rate at which two strands, corresponding to a full invader with a toehold of six bases and the 15-base toehold domain of the substrate, formed the intended 6-base-pair toehold. In one case we considered only native interstrand interactions, in the other we allowed all possible complementary base pairs. We found that allowing non-native base pairs increased association rates by approximately 50%, a small effect given the range of relative displacement rates considered in this work. More details are provided in the following sections.

The order parameter Q used for FFS up to the attachment of the invading strand to the substrate is the same for all toehold lengths, and the definition is given in Table S7. For this parameter, a potential correct base pair between the invading and substrate strands is counted as *nearly formed* if

- The separation of hydrogen bonding sites is $\leq$ 0.85 nm.
- The hydrogen-bonding potential consists of a separation dependent factor multiplied by a number of modulating angular factors. At most one of these factors that contributes multiplicatively to the hydrogen-bonding energy is zero.
- The hydrogen-bonding energy is less negative than $-2.98\,\mathrm{kcal\,mol^{-1}}$.

In this context, a 'correct' base pair is a base pair that is expected in the final substrate/invading strand duplex. Physically, these conditions mean that the bases are close and fairly well aligned, but not forming a strong base pair.

For higher values ($Q > 4$), the order parameter definition depends on toehold length. For shorter toeholds, a greater number of interfaces are needed to measure the flux accurately. Successive values of Q correspond to increasing numbers of correct base pairs (with a hydrogen-bonding energy more negative than $-2.98\,\mathrm{kcal\,mol^{-1}}$) between the invading strand and the substrate. Finally, the maximum value of Q corresponds to the invading strand having the maximum number of base pairs with the substrate, and all correct base pairs for the incumbent and substrate strand having a distance of at least 2.56 nm between hydrogen-bonding sites. The explicit definitions of $Q > 4$ for each toehold are given in Table S8.

For each toehold length, 100 independent simulations were performed to measure the initial flux. In

Duplex	Sequence (5′–3′)
Substrate	GACATGGAGA*CGTAGGGTATTGAATGAGGG*
Incumbent	T*CCCTCATTCAATACCCTACG*
Invader	*CCCTCATTCAATACCCTACG*[TCTCCAT]

Table S6: Sequences used in simulations of strand displacement. Bases in italics constitute the primary branch migration domain. The bases in square brackets indicate those that are added to create a toehold.

Order parameter Q	Separation d/nm	Nearly-formed bp n	Formed bp b
$Q = -2$	$d > 5.11$	0	0
$Q = -1$	$5.11 \geq d > 3.42$	0	0
$Q = 0$	$3.42 \geq d > 2.56$	0	0
$Q = 1$	$2.56 \geq d > 1.71$	0	0
$Q = 2$	$1.71 \geq d > 0.85$	0	0
$Q = 3$	$d \leq 0.85$	0	0
$Q = 4$	$d \leq 0.85$	$n \geq 1$	0

Table S7: Order parameter definitions for early stages of FFS simulations of displacement, up to the stage of attachment of the invading strand to the substrate. The separation d is the minimum distance between hydrogen-bonding sites over all potential correct base pairs in the invading and substrate strands.

Q	0,1	2	3	4
5	$b = 1$	$b = 1$	$1 \leq b < 3$	$1 \leq b < 4$
6	$2 \leq b < 4$	$2 \leq b < 5$	$3 \leq b < 8$	$4 \leq b$ & $Q \neq Q_{\max}$
7	$4 \leq b < 10$	$5 \leq b < 9$	$8 \leq b$ & $Q \neq Q_{\max}$	$Q = Q_{\max}$
8	$10 \leq b$ & $Q \neq Q_{\max}$	$9 \leq b$ & $Q \neq Q_{\max}$	$Q = Q_{\max}$	
9	$Q = Q_{\max}$	$Q = Q_{\max}$		

Q	5	6	7
5	$1 \leq b < 5$	$1 \leq b < 6$	$1 \leq b < 7$
6	$5 \leq b$ & $Q \neq Q_{\max}$	$6 \leq b$ & $Q \neq Q_{\max}$	$7 \leq b$ & $Q \neq Q_{\max}$
7	$Q = Q_{\max}$	$Q = Q_{\max}$	$Q = Q_{\max}$

Table S8: Order parameter definitions for the later stages of FFS simulations of displacement. b is the number of base pairs between substrate and invading strand with hydrogen-bonding energy more negative than $-2.98\,\mathrm{kcal\,mol^{-1}}$. $Q = Q_{\max}$ is defined as b having its maximum value (toehold length plus branch migration domain length) and all correct base pairs for the incumbent and substrate strand having a distance of at least 2.56 nm between hydrogen-bonding sites.

each simulation, 10 states at the interface λ^0_{-1} were collected, giving 1000 in total (a typical number in FFS simulations (24, 25)). Crossings of the λ^0_{-1} interface were saved with a 10 % probability, meaning that ~ 100 crossings were observed in total for each independent simulation. Saving states with only a 10 % probability ensures that the 1000 states collected are more statistically independent than otherwise. For each subsequent interface, a large number of trajectories were launched and those that reached the next interface before returning to $Q = -2$ were saved. The number of attempts and successes for each interface are given in Table S9.

Uncertainties in the measurements can be estimated in the following manner. As 100 independent simulations were performed for each toehold length to measure the initial flux, the standard error can be estimated in the usual way. Assuming we have obtained a representative set of states at each interface, the later stages can be modelled as Bernoulli trials – the probability of success measured after N attempts has a variance of $p(1-p)/N$, where p is the true probability of success. The measured p can then be used to estimate the standard error on p for each stage. The errors for individual stages can then be added in quadrature, and overall errors are given alongside the overall fluxes in Table S9. Note that this estimation of errors assumes that the set of states at each interface is a representative sample of the true distribution. As such, this error estimate is a lower bound on the true uncertainty. In particular, the assumption will be weakest for the 0-base toehold, where the number of completely independent reactive trajectories is small. However, given that the relative rates for different toehold lengths in the exponential regime are approximately consistent with what would be expected from the known thermodynamics of oxDNA, and that the overall difference between the shortest and longest toeholds is larger than six orders of magnitude, errors due to measurement uncertainty are unlikely to affect our conclusions.

In some simulations involving the longer toeholds, complete (and long-lived) binding to the toehold occurred during the initial measurements of the flux across λ^0_{-1}. In a conventional implementation of FFS (24, 25), the time spent in these states would be included in the estimate of the flux. As stated in the main text, however, for comparison to dilute systems we wish to ignore time spent in three-stranded complexes. Therefore these simulations were ended early, and the time spent bound to the toehold was disregarded. These binding events are not useless, however: the frequency with which they occurred can be compared to the predictions of FFS. The number of unsolicited binding events (9 in total for $\sim 0.63\,\mathrm{ms}$ of total simulation time for toeholds of length 4, 5, 6 and 7) is consistent with the predictions of FFS ($\sim 15\,\mathrm{ms}^{-1}$), suggesting that the implementation of FFS is reliable.

Simulations of association allowing non-native base pairs. We measured the rate at which two strands, corresponding to a full invader with a toehold of six bases and the 15-base toehold domain of the substrate (see Table S6) formed the intended 6-base-pair toehold, both with and without non-native interactions between the strands (intrastrand hairpins were allowed in both cases). The order parameters used, which are very similar to those used in the initial stages of the displacement simulations, and the results, are given in Table S10. 20 initial flux simulations were initialized for $0.86\,\mu\mathrm{s}$ each before sampling was started, and simulations that reached $Q = 7$ were restarted to avoid including the time taken to resolve a misbonded complex in the flux calculation (as such a time would be negligible compared to diffusional time scales at the low concentrations relevant to experiment). Errors are estimated analogously to those for displacement.

As can be seen from Table S10, although the rate of formation of structures with six base pairs is much faster when non-native interactions are present, many of these structures involve misbonds that subsequently melt. The overall result is that non-native interactions accelerate binding by only 50%, suggesting that the systematic effect of ignoring non-native base pairs on the relative rates of displacement for different toehold lengths is small.

Free energy profiles of displacement. Free energy profiles of displacement were sampled using VMMC simulations of the three strands at a temperature $T = 25^\circ\mathrm{C}$. In this work, the trial moves used to generate VMMC clusters were:

- Rotation of a nucleotide about its backbone site, with the axis chosen from a uniform random distribution and the angle from a normal distribution with mean of zero and a standard deviation of 0.12 radians.

- Translation of a nucleotide with the direction chosen from a uniform random distribution and the distance from a normal distribution with mean of zero and a standard deviation of 1.02 Å.

These trial moves are illustrated in Figure S12. The variances are chosen from experience to provide efficient sampling. Umbrella sampling was performed using a biasing of the system according to the number of base pairs between the substrate and the in-

Target interface	Toehold length 0	1	2	3
λ^0_{-1}	9581 (181 µs)	10400 (201 µs)	10532 (191 µs)	9851 (175 µs)
λ^1_0	10000 / 4031	10000 / 4406	10000 / 4187	10000 / 4264
λ^2_1	10000 / 4607	10000 / 4716	10000 / 4588	10000 / 4627
λ^3_2	10000 / 2304	10000 / 2468	10000 / 2635	10000 / 2721
λ^4_3	10000 / 1415	10000 / 1973	10000 / 2436	10000 / 2405
λ^5_4	50000 / 179	30000 / 745	25000 / 728	20000 / 765
λ^6_5	30000 / 526	15000 / 1877	3000 / 942	4500 / 1036
λ^7_6	60000 / 289	50000 / 315	16001 / 462	2000 / 261
λ^8_7	10000 / 1025	5000 / 325	2500 / 319	200 / 50
λ^9_8	300 / 149	300 / 131	300 / 92	
flux and error / s^{-1}	4.97×10^{-3} 6.5×10^{-4}	0.292 3.4×10^{-3}	7.06 0.89	210 31

Target interface	Toehold length 4	5	6	7
λ^0_{-1}	10179 (168 µs)	9859 (163 µs)	9617 (158 µs)	9148 (143 µs)
λ^1_0	10000 / 4316	10000 / 4497	10000 / 4229	10000 / 4327
λ^2_1	10000 / 4632	10000 / 4778	10000 / 4642	10000 / 4768
λ^3_2	10000 / 2732	10000 / 2920	10000 / 2999	10000 / 2966
λ^4_3	10000 / 2575	10000 / 2785	10000 / 3151	10000 / 3227
λ^5_4	20000 / 797	10000 / 408	10000 / 490	10000 / 490
λ^6_5	3000 / 767	3000 / 967	1000 / 289	1000 / 290
λ^7_6	200 / 51	199 / 177	100 / 100	100 / 100
flux and error / s^{-1}	2.22×10^3 300	1.24×10^4 840	1.61×10^4 1.2×10^3	1.81×10^4 1.4×10^3

Table S9: Trajectories attempted/successful at each stage of FFS for all toehold lengths. For λ^0_{-1}, values are given for the total number of trajectories crossing λ^0_{-1} (for the first time since leaving $Q = -2$), and the total simulation time taken. The interfce corresponding to the formation of the first base pair is highlighted in yellow, and the interface corresponding to the formation of the full toehold in green (when this is distinct from the first bp).

Order parameter Q	Definition	Native interactions only	Non-native interactions permitted
$Q=-2$	$d>5.11$		
$Q=-1$	$5.11\geq d>3.42$	Crossings of λ^0_{-1} (simulation time / µs)	
$Q=0$	$3.42\geq d>2.56$	8195 (69.3)	8145 (66.9)
		Attempts/successes at reaching λ^Q_{Q-1} from λ^{Q-1}_{Q-2}	
$Q=1$	$2.56\geq d>1.71$	10000/4327	10000/4416
$Q=2$	$1.71\geq d>0.85$	10000/5186	10000/5167
$Q=3$	$0.85\geq d$ & $n=0$	10000/5333	10000/5152
$Q=4$	$n\geq 1$ & $b=0$ & $c=0$	10000/968	10000/5333
$Q=5$	$b=1$ & $c=0$	12000/852	12000/2094
$Q=6$	$b\geq 2$ & $6>c\geq 1$	7500/3468	12000/3213
$Q=7$	$c\geq 6$ [& $c_{\rm nat}<c$]	2500/1879	5850/2251
$Q=8$	$c\geq 6$ & $c_{\rm nat}=c$		277/104
		Overall flux (and error) / s^{-1}	
		3.83×10^4 (1.57×10^3)	5.15×10^4 (3.28×10^3)

Table S10: Order parameter definitions FFS simulations of association for an invader with a 6-base toehold and the 15-base toehold domain of the substrate, and simulation results. The separation d is the minimum distance between hydrogen-bonding sites over *all* pairs of bases in the invading and substrate strands. n is the number of nearly formed base pairs, as defined in the text. b is the number of base pairs with energy more negative than $-1.43\,\mathrm{kcal/mol}$, and c the number of base pairs with energy more negative than $-1.79\,\mathrm{kcal/mol}$. $c_{\rm nat}$ is the number of those base pairs which are native (i.e., the intended toehold base pairs). In the native-only simulations, $c_{\rm nat}=c$ by definition, and $Q=7$ is the maximal value in this case.

cumbent strand, and the substrate and the invading strand. The umbrella biasing potential forbade complete detachment of any strand. States were recorded in histograms according to the intact base pairs between invading and substrate strands closest to the $3'$ end of the substrate. Further, states were divided between coaxially stacked and unstacked macrostates according to the configurations of the nucleotides between the final base to which the invading strand was paired and the first base to which the incumbent was bound. If any of these substrate bases was not stacked with its neighbour, the state was deemed to be coaxially unstacked. For the purpose of these simulations, an interaction energy (hydrogen-bonding or stacking energy) more negative than $-0.60\,\mathrm{kcal\,mol^{-1}}$ was counted as an instance of hydrogen-bonding or stacking, as appropriate. Final data was obtained from 10 simulations of 4×10^{10} attempted VMMC moves.

Duplex formation. To measure the effect of ssDNA overhangs on melting equilibria, simulations of the hybridization of a strand to the single-stranded overhang of a hairpin were performed. Dangling poly(dT) overhangs of various lengths were included to indicate the destabilizing effect of excess ssDNA at a junction. Hairpin stems of length 12, with a loop of length 6, were used. Complementary sections of length 6 and 8 were used to allow accurate estimates of the destabilization at 25°C and 55°C. The sequences used are provided in Table S11.

In this case, all complementary base pairs were allowed to form hydrogen bonds. VMMC simulations were performed in periodic simulation cells of volume 1.67×10^{-20}l at a range of temperatures in the vicinity of 25°C and 55°C. Histogram reweighting (27) was used to infer the results at the desired temperatures. 4 simulations of 4×10^{10} steps each were performed in a periodic cubic cell of volume $3.96\times10^{20}\,\mathrm{l}$ for each system, with attempted moves identical to those used for the displacement landscape (except that rotations were drawn from a distribution with a standard deviation of 0.2 radians and displacements from a distribution with standard deviation 1.7 Å) . Umbrella sampling as a function of the number of interstrand base pairs was used to accelerate sampling. The ratio of bound to unbound states in simulations, ϕ, was recorded (any state with at least one interstrand hydrogen-bond more negative than $-0.60\,\mathrm{kcal\,mol^{-1}}$ was counted as bound). The free-energy of formation follows as $\Delta G=-RT\ln\phi$: values for various combinations of ssDNA overhangs are reported in Table 2. For each system, free energies inferred from

Molecule	Sequence
Hairpin	5′-(TTTTTTTTTT) [GTACATCTGAAG] TTTTTT [CTTCAGATGTAC] TACCGT{AG}-3′
ssDNA	5′- {CT}ACGGTA(TTTTTTTTTT) -3′

Table S11: Sequences used in simulations of the hybridization of a strand to the single-stranded overhang of a hairpin to measure the effect of ssDNA overhangs on melting equilibria. Bases in brackets "()" represent the overhangs, which are not present in every simulation. Bases enclosed by "{}" are only used in simulations of the 8-base hybridization. Square brackets "[]" enclose the stem of the sequence.

the 4 separate simulations were consistent to within $\sim 0.1\,\mathrm{kcal\,mol^{-1}}$.

S7 Notes on 1D Landscape Models

A sequence-dependent free energy landscape for RNA strand displacement. Figure S14 shows the sequence-dependent free energy landscape for strand displacement with a 10-base toehold at 25°C predicted by *efn2* (28, 29). From this we infer that their model accounts for junction-context only when the junction is part of an 'interior multiloop'; during branch migration, the overhangs at the junction form an 'exterior loop', for which it appears that the coaxial stacking terms are not calculated.

Comparing IEL predictions to a prior phenomenological model. We present below the formulae derived by Zhang and Winfree (1) using their phenomenological model of reversible toehold exchange, restricted to the irreversible strand displacement case. We use their equations 1 and 2, in the limit where the 0-length "reverse toehold" dissociation rate is arbitrarily large, as further described in their Figure 8. Denoting their effective bimolecular rate constant for strand displacement by $k_{\mathrm{eff}}^{\mathrm{ZW}}(h)$, we have

$$k_{\mathrm{eff}}^{\mathrm{ZW}}(h) \approx \frac{k_f\ k_b}{k_{\mathrm{rev}}(h) + k_b} \tag{81}$$

where

$$k_{\mathrm{rev}}(h) \approx \frac{2\ k_f}{b} e^{-|\Delta G^\circ(h)|/RT} \tag{82}$$

and

$$k_b \approx \frac{400}{b^2}. \tag{83}$$

$k_f \approx 3 \times 10^6$ /M/s is their fitted rate constant for toehold hybridization, k_b is their fitted rate constant for crossing the "half-way point" of branch migration, $k_{\mathrm{rev}}(h)$ is the calculated unimolecular rate constant for toehold dissociation, b is the length of the branch migration domain, and $|\Delta G^\circ(h)|$ is the absolute free energy of binding between the toehold and its complement.

We compared the dependence of strand displacement kinetics on branch migration domain length as predicted by IEL(5.3, 2.0) and the phenomenological model of Zhang and Winfree (1) (Figure S15). Numerically, predictions of their phenomenological model are quite consistent with the IEL's predictions in the cases we examined.

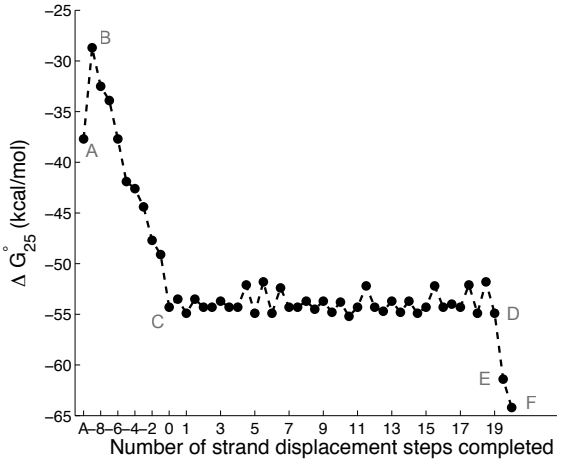

Figure S14: The sequence-dependent free energy landscape of strand displacement for a 10-base toehold at 25°C predicted by *efn2* for RNA molecules. States A–F correspond to those in the IEL analysis, Figure 3 of the main text.

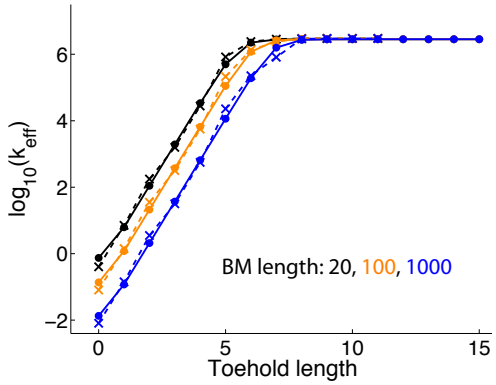

Figure S15: Predicted dependence of k_{eff} on toehold length for various lengths of the branch migration domain. IEL(5.3, 2.0)'s predictions are marked by filled circles and solid lines, while predictions of the phenomenological model of Zhang and Winfree (1) are indicated by crosses and dashed lines.

References

[1] D. Zhang and E. Winfree, "Control of DNA strand displacement kinetics using toehold exchange," *J. Am. Chem. Soc.*, vol. 131, no. 47, pp. 17 303–17 314, 2009.

[2] G. Rudolph, "The fundamental matrix of the general random walk with absorbing boundaries." Collaborative Research Center "Computational Intelligence" CI-75, University of Dortmund, Tech. Rep., 1999.

[3] K. Kawasaki, "Diffusion constants near the critical point for time-dependent ising models." *Phys. Rev.*, vol. 145, pp. 224–230, 1966.
[4] N. Metropolis, A. W. Rosenbluth, M. N. Rosenbluth, A. H. Teller, and E. Teller, "Equation of state calculation by fast computing machines." *J. Chem. Phys.*, vol. 21, no. 6, pp. 1087–1092, 1953.
[5] W. Feller, *An introduction to probability theory and its applications*. New York: Wiley and Sons, 1968, vol. 1.
[6] C. M. Radding, K. L. Beattie, W. K. Holloman, and R. C. Wiegand, "Uptake of homologous single-stranded fragments by superhelical DNA," *J. Mol. Biol.*, vol. 116, pp. 825–839, 1977.
[7] C. Green and C. Tibbetts, "Reassociation rate limited displacement of DNA strands by branch migration," *Nucl. Acids Res.*, vol. 9, no. 8, pp. 1905–1918, 1981.
[8] D. T. Gillespie, "Exact stochastic simulation of coupled chemical reactions," *J. Phys. Chem.*, vol. 81, no. 25, pp. 2340–2361, 1977.
[9] J. M. Schaeffer, "Stochastic simulation of the kinetics of multiple interacting nucleic acid strands," Ph.D. dissertation, California Institute of Technology, 2013.
[10] S. Bommarito, N. Peyret, and J. SantaLucia, Jr., "Thermodynamic parameters for DNA sequences with dangling ends," *Nucl. Acids Res.*, vol. 28, no. 9, pp. 1929–1934, 2000.
[11] J. N. Zadeh, C. D. Steenberg, J. S. Bois, B. R. Wolfe, M. B. Pierce, A. R. Khan, R. M. Dirks, and N. A. Pierce, "NUPACK: analysis and design of nucleic acid systems," *J Comput. Chem.*, no. 32, pp. 170–173, 2011.
[12] R. M. Dirks, J. S. Bois, J. M. Schaeffer, E. Winfree, and N. A. Pierce, "Thermodynamic analysis of interacting nucleic acid strands," *SIAM Review*, vol. 49, no. 1, pp. 65–88, 2007.
[13] M. Zuker, "Mfold web server for nucleic acid folding and hybridization prediction," *Nucl. Acids Res.*, vol. 31, no. 13, pp. 3406–3415, 2003.
[14] I. L. Hofacker, "Vienna RNA secondary structure server," *Nucl. Acids Res.*, vol. 31, no. 13, pp. 3429–3431, 2003.
[15] J. D. Puglisi and I. T. Jr., "Absorbance melting curves of RNA," *Methods Enzymol.*, vol. 180, pp. 304–325, 1989.
[16] D. D. Albergo, L. A. Marky, K. J. Breslauer, and D. H. Turner, "Thermodynamics of (dG-dC)$_3$ double-helix formation in water and deuterium oxide," *Biochemistry*, vol. 20, no. 6, pp. 1409–1413, 1981.
[17] A. Gelman, J. B. Carlin, H. S. Stern, and D. B. Rubin, *Bayesian Data Analysis*. CRC Press, 2004.
[18] T. E. Ouldridge, "Coarse-grained modelling of DNA and DNA nanotechnology," Ph.D. dissertation, University of Oxford, 2011.
[19] J. SantaLucia, Jr., "A unified view of polymer, dumbbell, and oligonucleotide DNA nearest-neighbor thermodynamics." *Proc. Natl. Acad. Sci. U.S.A*, vol. 17, no. 95(4), pp. 1460–5, 1998.
[20] S. Whitelam, E. H. Feng, M. F. Hagan, and P. L. Geissler, "The role of collective motion in examples of coarsening and self-assembly," *Soft Matter*, vol. 5, no. 6, pp. 1521–1262, 2009.
[21] S. Whitelam and P. L. Geissler, "Avoiding unphysical kinetic traps in Monte Carlo simulations of strongly attractive particles," *J. Chem. Phys.*, vol. 127, p. 154101, 2007.
[22] G. M. Torrie and J. P. Valleau, "Nonphysical sampling distributions in monte carlo free-energy estimation: Umbrella sampling," *J. Comp. Phys.*, vol. 23, pp. 187–199, 1977.
[23] R. L. Davidchack, R. Handel, and M. V. Tretyakov, "Langevin thermostat for rigid body dynamics," *J. Chem. Phys.*, vol. 130, no. 23, p. 234101, 2009.
[24] R. J. Allen, P. B. Warren, and P. R. ten Wolde, "Sampling rare switching events in biochemical networks," *Phys. Rev. Lett.*, vol. 94, no. 1, p. 018104, 2005.
[25] R. J. Allen, C. Valeriani, and P. R. ten Wolde, "Forward flux sampling for rare event simulations," *J. Phys.: Condens. Matter*, vol. 21, no. 46, p. 463102, 2009.
[26] T. E. Ouldridge, P. Šulc, F. Romano, J. P. K. Doye, and A. A. Louis, "DNA hybridization kinetics: zippering, internal displacement and sequence dependence," *arxiv:1303.3370*, 2013.
[27] A. M. Ferrenberg and R. H. Swendsen, "New Monte Carlo technique for studying phase transitions," *Phys. Rev. Lett.*, vol. 61, pp. 2635–2638, 1988.
[28] D. H. Mathews, J. Sabina, M. Zuker, and D. H. Turner, "Expanded sequence dependence of thermodynamic parameters improves prediction of RNA secondary structure," *J. Mol. Biol.*, vol. 288, no. 5, pp. 911–940, 1999.
[29] D. H. Mathews, M. D. Disney, J. L. Childs, S. J. Schroeder, M. Zuker, and D. H. Turner, "Incorporating chemical modification constraints into a dynamic programming algorithm for prediction of RNA secondary structure," *Proc. Natl. Acad. Sci. U.S.A*, vol. 101, no. 19, pp. 7287–7292, 2004.